

How do modeling choices and erosion zone locations impact the representation of connectivity and the dynamics of suspended sediments in a multi-source soil erosion model?

Magdalena Uber¹, Guillaume Nord¹, Cédric Legout¹, Luis Cea.²

¹Univ. Grenoble Alpes, CNRS, IRD, Grenoble INP, IGE, 38000 Grenoble, France

²Environmental and Water Engineering Group, Department of Civil Engineering, Universidade da Coruña, A Coruña,

Correspondence to: Cédric Legout (cedric.legout@univ-grenoble-alpes.fr) France

1. Abstract

Soil erosion and suspended sediment transport understanding is an important issue in terms of soil and water resources management in the critical zone. In mesoscale watersheds (>10km²) the spatial distribution of potential sediment sources within the catchment associated to the rainfall dynamics are considered as the main factors of the observed suspended sediment flux variability within and between runoff events. Given the high spatial heterogeneity that can exist for such scales of interest, distributed physically based models of soil erosion and sediment transport are powerful tools to distinguish the specific effect of structural and functional connectivity on suspended sediment flux dynamics. As the spatial discretization of a model and its parameterization can crucially influence how structural connectivity of the catchment is represented in the model, this study analyzed the impact of modeling choices in terms of contributing drainage area (CDA) threshold to define the river network and of Manning's roughness parameter (n) on the sediment flux variability at the outlet of two geomorphological distinct watersheds. While the modeled liquid and solid discharges were found to be sensitive to these choices, the patterns of the modeled source contributions remained relatively similar when the CDA threshold was restricted to the range of 15 to 50 ha, n on the hillslopes to the range 0.4-0.8 and to 0.025-0.075 in the river. The comparison of both catchments showed that the actual location of sediment sources was more important than the choices made during discretization and parameterization of the model. Among the various structural connectivity indicators used to describe the geological sources, the mean distance to the stream was the most relevant proxy of the temporal characteristics of the modeled sedigraphs.

2. Introduction

Soil erosion and suspended sediment transport are natural processes that can be exacerbated by human activities and are thus a major concern for soils and water resources management. They cause on- and off-site effects such as the loss of fertile top soil, muddy flooding, freshwater pollution due to the preferential transport of adsorbed nutrients and contaminants, increased costs for drinking water treatment, reservoir siltation and aggression of fish respiratory systems (Owens et al., 2005; Brils, 2008; Boardman et al., 2019). Although these problems are already important in the Mediterranean and mountainous context (Vanmaercke et al., 2011), questions arise about the future evolution of suspended sediment yields due to the expected increase on the intensity and frequency of severe

37 precipitation events in the following decades in these areas (Alpert et al., 2002; Trambly et al., 2012; Blanchet et
38 al., 2018).

39 In mesoscale catchments (<100 km²), which correspond to a relevant scale for decision makers, correct modeling
40 of the hydrosedimentary responses requires a good understanding of the interactions between the spatiotemporal
41 dynamics of the rainfall with the spatial distribution of the catchment geomorphological characteristics. Several
42 studies have shown that the contributions of potential sediment sources can differ considerably from one flood
43 event to another and at different times of sampling within a flood event (Brosinsky et al., 2014 ; Gourdin et al.,
44 2014; Cooper et al., 2015; Gellis and Gorman Sanisaca, 2018; Vercruyssen and Grabowski, 2019), particularly in
45 watersheds with a Mediterranean or mountainous climate (Evrard et al., 2011 ; Navratil et al., 2012; Poulenard et
46 al., 2012; Legout et al., 2013; Uber et al., 2019). Possible reasons for the observed variability of suspended
47 sediment fluxes from one event to another include seasonal variations of the climatic drivers of soil erosion and
48 sediment transport, variability of the spatial distribution of rainfall, land cover changes and human interventions
49 (Vercruyssen et al., 2017). At the event scale, the distribution of sources within the catchment and thus different
50 travel times of sediment from sources to the outlet as well as rainfall dynamics are assumed to be the dominant
51 reason for the observed suspended sediment flux variability (Legout et al., 2013).

52 Thus, the dynamics of suspended sediment fluxes during one event are hypothesized to result from the interplay
53 of structural and functional connectivity of the sources in the catchment. Wainwright et al. (2011) define structural
54 connectivity as the “extent to which landscape units are contiguous or physically linked to one another”. In the
55 context of soil erosion and sediment transfer studies it is of interest how active erosion zones are linked to the
56 catchments outlet. Structural connectivity can be measured using indices of contiguity (Heckmann et al., 2018). It
57 is an intrinsic property of the landscape, that usually does not consider interactions, directionality and feedbacks.
58 Functional connectivity on the other hand, specifically describes the linkage of landscape units by processes that
59 depend e.g. on the characteristics of rain events. While some recent studies have shown the benefits of using the
60 concepts of structural and functional connectivity to understand the spatial and temporal variability of sediment
61 fluxes (Cossart et al., 2018; Lopez-Vicente and Ben-Salem, 2019), distinguishing both concepts remains
62 challenging (Wainwright et al., 2011).

63 Distributed physically based models of soil erosion and sediment transport are powerful tools to distinguish the
64 specific effect of structural and functional connectivity on suspended sediment flux dynamics. Some recent studies
65 have already combined erosion and sediment transport modeling with sediment fingerprinting data (Theuring et
66 al., 2013; Wilkinson et al., 2013; Palazón et al., 2014, 2016; Mukundan et al., 2010a, 2010b). However, all of these
67 studies focused on long term mean source contributions, without working at high temporal resolution to understand
68 the dynamics of suspended sediment fluxes within and between flood events. Yet, numerical models can help to
69 understand the effect of the distribution of sources within the catchment, their linkage to the outlet, their travel
70 times and the characteristics of the rain events on the variability of suspended sediment source contributions
71 observed at the outlet.

72 The fact is that modeling soil erosion and sediment transport remains a challenge as there is no optimal model to
73 represent all erosion and hydrological processes in the catchment and there is no standard protocol for the choice
74 and set-up of the model (Merrit et al., 2003; Wainwright et al., 2008). Indeed, the outputs of hydro-sedimentary
75 models are very sensitive to choices made by the modeler in the way that processes are selected and spatially
76 implemented, as well as during model discretization, parametrization, forcing and initialization (Merrit et al.,

2003). We consider especially that the spatial structure and the discretization of the model, as well as its parameterization can crucially influence how structural connectivity of the catchment is represented in the model. In mesoscale catchments, the connectivity of sources to the outlet depends a lot on the distance to the stream. In many cases, however, the definition of the stream is not unambiguous (Tarboton et al., 1991, Turcotte et al., 2001). In most cases, the river network is based on topographic analysis in GIS software, where a stream is made up of all the cells of the digital elevation model (DEM) that exceed a threshold of contributing drainage area (CDA, Tarboton et al., 1991; Colombo et al., 2007). The CDA of a DEM cell is the cumulative size of all cells that are located upstream of the given cell and that drain into that cell. Thus, the definition of the stream and in consequence the connectivity of active erosion sources to the outlet is highly dependent on the choice of the CDA threshold (Colombo et al., 2007). Concerning parameterization, travel times of the sources to the outlet and thus structural connectivity also depend on how surface water and sediment fluxes are calculated and parameterized. Many distributed models such as WEPP (Lafren et al., 1991), KINEROS (Woolhiser et al., 1990) and MIKE 11 (Hanley et al., 1998) use the depth-integrated shallow water equations (St. Venant equations) or different approximations of them, as the kinematic or the diffusive wave approximations, for routing surface water to the outlet of the catchment (Pendey et al., 2016). These equations are highly sensitive to the roughness parameter, which values depend whether shallow water with partial inundation on hillslopes or concentrated flow in rivers are modeled (Baffaut et al., 1997; Tiemeyer et al., 2007; Fraga et al., 2013, Cea et al., 2016). This paper contributes to improve our understanding of the hydrosedimentary processes in the catchment that lead to sediment flux variability at the outlet. We focus on the role of structural connectivity using a distributed physical based model, applied to two mesoscale Mediterranean catchments. Since model outputs are supposed to be highly sensitive to the choices made during model set-up, the first objective is to assess the impact of the choices made during model discretization and parameterization on modeled suspended sediment flux dynamics. A second objective is to assess how structural connectivity, particularly the location of the sediment sources, impacts modeled suspended sediment flux dynamics for both catchments.

101 **3.Methods**

102 **3.1.Characteristics of the modeled study sites**

103 **3.1.1 Catchment description**

104 Both study sites are long term research observatories belonging to the French network of critical zone observatories (OZCAR, Gaillardet et al., 2018).

106 The 42 km² Claduègne catchment is a tributary of the Auzon river in Southeastern France. Being part of the Cévennes-Vivarais Mediterranean Hydrometeorological Observatory (OHMCV, Boudevillain et al., 2011), the catchment is a research site dedicated to the investigation of meteorological and hydrosedimentary processes during heavy rain events and flash floods (Braud et al., 2014; Nord et al., 2017). The climate is dominated by Mediterranean and oceanic influences with heavy rain events occurring mostly in autumn and to a lesser extent in spring, and localized thunderstorms occurring more rarely in summer. These intense rain events can cause flash floods and high sediment export. Average annual precipitation is 1050 mm (Huza et al., 2014). The geology of the catchment is composed of basalts in the northern part and sedimentary rocks in the southern part. Uber et al. (2019) identified three sources of suspended sediment: i) marly calcareous badlands are the major source of suspended sediments due to their erodibility and connectivity to the river network, ii) diffuse sources on basaltic geology comprising cultivated fields (mainly cereals) that are temporarily bare and iii) diffuse sources on sedimentary

117 geology equally comprise cultivated fields (mainly cereals) and vineyards where bare soil is found in between the
118 rows of the vine plants (Figure 1a). Table 1 gives the surface and the slopes of the catchment and the erosion zones.
119 The 20 km² Galabre catchment is a headwater catchment of the Bléone river located in the southern French alps
120 (Figure 1b). It is part of the Draix-Bléone Observatory dedicated to the study of hydrology and erosive processes
121 in a mountainous context with extensive badlands. The climate of the Galabre catchment, whose altitude varies
122 between 735 and 1909 m, is impacted by Mediterranean and mountainous influences with a mean annual
123 precipitation of around 1000 mm. There is a high seasonality with most precipitation occurring in spring and
124 autumn, although thunderstorms with high rain intensity also occur in summer (Esteves et al., 2019). The
125 catchment is entirely located on sedimentary rocks comprising limestones (34%), marls and marly limestones
126 (30%), gypsum (9%), molasses (9%) and Quaternary deposits (18%). A prominent feature of the catchment are
127 the badlands, that are found on all five types of rock and cover about 9.5% of the surface of the catchment (Esteves
128 et al., 2019). The land use is dominated by forests and scrublands, which are permanently covered by vegetation
129 and are thus assumed to be negligible as sediment sources. Agricultural zones are barely present in the catchment.
130 Suspended sediment fingerprinting studies revealed that most of the sediments originate from the badlands of
131 molasses and marls (Poulenard et al., 2012; Legout et al., 2013). Table 1 gives the characteristics of the catchment.
132 In comparison, the Galabre catchment is smaller and steeper than the Claduègne catchment. The distribution of
133 the erosion zones differs in the two catchments, with the ones in the Galabre catchment being more dispersed over
134 the entire catchment but smaller in size due to the absence of diffuse agricultural sources.
135 Liquid and solid fluxes are continuously monitored at the outlets of both catchments with the same sensors and
136 protocols, from which suspended sediment yields are calculated (Table 1). Water level is measured with an H-
137 radar and converted to discharge with a stage discharge rating curve. Suspended sediment concentrations are
138 monitored with turbidimeters and suspended sediment samples are automatically taken every 40 min once a
139 threshold of turbidity and water level is exceeded. These samples are dried and weighed and are used to establish
140 a rating between turbidity and suspended sediment concentrations.

141
142 3.1.2 Connectivity indicators In order to quantify the structural connectivity of the sources in the catchments, four
143 indicators were calculated, i.e. the distance to the outlet, distance to the stream and the two indices of connectivity
144 (IC) proposed by Borselli et al. (2008) and Cavalli et al. (2013). The distance to the outlet metric refers to the
145 width function and is applied as a measure of network structure and catchment shape by Hancock et al. (2010).
146 Maps of the distance to the outlet along the flowlines (i.e. the distance that water and sediments travel following
147 the gradient of the terrain elevation) and the distance to the stream were created. For the latter, the stream network
148 obtained with a CDA threshold of 50 ha was used. The distance to the outlet and the distance to the stream of a
149 given position in the catchment serve as proxies of longitudinal (upstream-downstream) and lateral (hillslope-
150 channel) connectivity in the sense of Fryirs (2013). Both maps were created using TauDEM (Tarboton, 2010) and
151 a digital elevation model at a resolution of 1m (Claduègne: bare earth Lidar DEM, Nord et al., 2017; Galabre:
152 RGE ALTI product of IGN, 2018). However, neither of these measures takes into account surface roughness and
153 slope. Thus, two of the most widely used indicators of connectivity, i.e. the IC proposed by Borselli et al. (2008)
154 and the adjusted version of IC proposed by Cavalli et al. (2013), were calculated. Both indicators were calculated
155 for each pixel of the DEM and take into account the CDA of that pixel and the distance to the stream along the
156 flow lines. They also both include a weighting factor for the mean slope in the CDA and along the downstream

157 path as well as a second weighting factor W . Borselli et al. (2008) weight the index with land use, thus the factor
 158 W was derived from the values proposed by Panagos et al. (2015) for the land use data that was obtained from
 159 Inglada et al. (2017). Cavalli et al (2013) on the other hand propose a roughness index as the weighting factor W
 160 that represents a local measure of topographic surface roughness that is calculated for a 5 x 5 cell moving window.
 161 Both indicators were calculated using the program SedInConnect (Crema and Cavalli, 2017). All these four
 162 indicators were calculated for each pixel within the catchments and their values on the erosion zones were
 163 extracted. Mean values and standard deviations are given in Table 1, while the distributions of the distance to the
 164 outlet and to the stream are shown in Figure 2. These characteristics of the catchments indicate that not only
 165 erodibility but also structural connectivity differs strongly between the two catchments and between sources.

166 **3.2. Model description**

167 Surface runoff, soil erosion and sediment transport in the study catchments were modeled with an ad-hoc version
 168 of the software Iber (Bladé et al., 2014) developed in a previous study by the authors (Cea et al. 2016). A detailed
 169 description of the model and numerical schemes is beyond the scope of this paper and can be found in previous
 170 publications. Thus, just a brief description of the model equations is presented in the following.

171 **Hydrodynamic module**

172 Water depth and velocity fields are computed from the solution of the 2D depth-averaged shallow water equations
 173 applied to the whole catchment domain (including hillslope and channel). Including rainfall and infiltration terms
 174 as well as Manning's formula for bed friction the hydrodynamic equations solved by the model can be written as:

$$\begin{aligned}
 175 \quad & \frac{\partial h}{\partial t} + \frac{\partial q_x}{\partial x} + \frac{\partial q_y}{\partial y} = R - I \\
 176 \quad & \frac{\partial q_x}{\partial t} + \frac{\partial}{\partial x} \left(\frac{q_x^2}{h} \right) + \frac{\partial}{\partial y} \left(\frac{q_x q_y}{h} \right) = -gh \frac{\partial z_s}{\partial x} - g \frac{n^2}{h^{7/3}} |q| q_x \\
 177 \quad & \frac{\partial q_y}{\partial t} + \frac{\partial}{\partial x} \left(\frac{q_x q_y}{h} \right) + \frac{\partial}{\partial y} \left(\frac{q_y^2}{h} \right) = -gh \frac{\partial z_s}{\partial y} - g \frac{n^2}{h^{7/3}} |q| q_y
 \end{aligned} \tag{1}$$

178 where h is the water depth, t is time, q_x and q_y are the components of the unit discharge in the two horizontal
 179 directions, R is the rainfall intensity, I is the infiltration rate, g is gravity acceleration, z_s is the elevation of the free
 180 surface and n is Manning's roughness parameter. The shallow water equations are solved with an unstructured
 181 finite volume solver developed in Cea and Bladé (2015) for rainfall runoff applications at the catchment scale. The
 182 solver is explicit in time, meaning that the maximum time step that can be used to evolve the equations in time is
 183 limited by the Courant-Friedrichs-Lewy (CFL) condition (Courant et al. 1967). This implies that the time step in
 184 typical applications is of the order of one second or less. The CFL condition is implemented in the solver and thus,
 185 the computational time step is automatically evaluated from the grid size, water velocity and water depth.

186 **Soil erosion module**

187 A full description of the soil erosion model can be found in Cea et al. (2016). The complete soil erosion model
 188 uses a two-layer soil structure that consists of one layer of eroded material over a layer of non-eroded cohesive
 189 soil. Different sediment classes, each one with its own physical properties, can be considered and routed with the
 190 model.

191 Given the results of Cea et al. (2016) that the two-layer structure of the model increases its complexity without
 192 significantly improving its predictive capacity in real applications, we only use a single-layer structure with
 193 vertically uniform erodibility. We assume that the single-layer structure is adequate for the badlands where there
 194 usually is a thick regolith layer, and erosion from the underneath cohesive layer is negligible compared to the one

195 of the regolith layer. In the complete model, two particle detachment processes are considered, i.e. rainfall-driven
 196 detachment and flow-driven entrainment. In our case, we assume that rainfall-driven detachment is the most
 197 significant of both processes and thus, it is the only detachment mechanism considered in our simulations. We
 198 further assume that all eroded particles are transported in suspension to the outlet and that deposition is negligible.
 199 This wash load hypothesis leads to a further simplification of the erosion module compared to the original one
 200 proposed by Cea et al. (2016), i.e. the omission of the deposition term. Given the previous assumptions, the soil
 201 erosion model used in this work solves the following mass conservation equation for each sediment class
 202 considered:

$$\frac{\partial h c_s}{\partial t} + \frac{\partial q_x c_s}{\partial x} + \frac{\partial q_y c_s}{\partial y} = D_{rdd,s} \quad s = 1, N_c$$

(2)

206 where N_c is the number of sediment classes, C_s [kg m^{-3}] is the depth-averaged concentration of the sediment class
 207 s and $D_{rdd,s}$ [$\text{kg m}^{-2} \text{s}^{-1}$] is the rainfall-driven detachment rate for the sediment class s . The rainfall-driven
 208 detachment is calculated assuming a linear relationship between the detachment rate and the rain intensity, i.e.
 209 $D_{rdd,s} = \alpha_s R$, where α_s [$\text{g mm}^{-1} \text{m}^{-2}$] is the rainfall erodibility coefficient for the sediment class s and represents the
 210 mass flux detached per unit area by a unit rainfall intensity. Thus, the suspended sediment concentration at every
 211 time step and location is calculated from Eq. 2, which is a simplified version of the equation given in Cea et al.
 212 (2016) for the case where a single-layer structure, only rainfall-driven detachment and no deposition are assumed.
 213 Eq. 2 is solved with an unstructured finite volume solver using the same spatial discretisation as for the
 214 hydrodynamic equations. For a detailed description of the numerical schemes used to solve Eq. 2 coupled to the
 215 shallow water equations the reader is referred to Cea and Vázquez-Cendón (2012). The solution of Eq. 2 allows
 216 us to compute the concentration, and thus the mass fluxes (as the product of the concentration times the unit
 217 discharge) of each sediment class at any time and location in the catchment, and in particular, the contribution of
 218 each sediment class to the total sedigraph computed at the basin outlet.

219

220 3.3. Model discretization and input data

221 As a distributed model, Iber requires a computational mesh which is made up by three main modeling units with
 222 different spatial discretization and roughness coefficients, i.e. the river network, the hillslopes and the badlands.
 223 The river bed was delineated by i) identifying the river network using TauDEM (Tarboton, 2010) and ii) creating
 224 a polygon by "buffering" the line feature of the river. In order to take into account that the width of the river varies
 225 from upstream to downstream, we introduced a distinction between the perennial river network defined using a
 226 CDA of 500 ha and the intermittent river network obtained using a CDA of 15 ha. While the highest value of 500
 227 ha is often used for cartography and large scale modeling studies (e. g. Colombo et al., 2007; Vogt et al., 2007;
 228 Bhowmik et al., 2015), the smallest value of 15 ha was found to create a river network that includes the intermittent
 229 streams observed in the catchment. For the former a buffer of 10 m to both sides of the river was applied. For the
 230 latter, composed of small tributaries and in good agreement with field observations of the whole extension of the
 231 hydrographic network during floods, a buffer of 5 m was applied. The badlands were delineated based on
 232 orthophotos and verified during field trips, while the hillslopes cover the rest of the catchments. While the badlands
 233 are a part of the hillslopes in terms of geomorphology and hydraulics, we differentiated them here to be able to
 234 apply a different parameterization and discretization.

235 These principal modeling units were discretized as a finite volume mesh. In our study, we used an unstructured
236 triangular mesh with variable mesh size in the different units. The smallest mesh size was required in the modeling
237 unit “river network”, where water and sediment fluxes are concentrated, so it was set to 5 m. In the modeling unit
238 “hillslopes” a coarser mesh size of 100 m was chosen in order to reduce the number of elements and thus
239 computation time. In the modeling unit “badlands”, where the fluxes are concentrated in the steep gullies, an
240 intermediate mesh size of 20 m was used. At the border between two modeling units the mesh size evolves
241 gradually. With this discretization the model of the Claduègne consists of roughly 173.000 mesh elements, while
242 the one of the Galabre catchment of 75.000 elements. Values for Manning's and erodibility were assigned to each
243 mesh element. The Manning's roughness parameter was uniform in each modeling unit but could vary from one
244 scenario to another with values ranging from 0.025 to 0.1 in the “river network” and from 0.2 to 0.8 in “hillslopes”
245 and “badlands”. It was chosen that the domain would get two Manning's values (channel vs hillslope), i.e a value
246 for the modeling unit “river network” and another value for the modeling units “hillslopes” and “badlands”.
247 While runoff is generated and routed in the entire catchment, the production of sediment was limited to the
248 potential erosion zones. The latter include all the mesh elements in the modeling unit “badlands” and the mesh
249 elements of the “hillslopes” modeling unit that belonged to the diffuse agricultural sources in the Claduègne
250 catchment. The erosion zones were classified according to i) their geology, i.e. in three classes for the Claduègne
251 and four for the Galabre catchment (Figure 1), ii) their geology and their distance to the outlet (Figure 2a,c) and
252 iii) their geology and their distance to the stream network (Figure 2b,d). Sediment production ($D_{rdd,s}$) was
253 calculated in each mesh element of the potential erosion zones for each source class separately. Sediment transfer
254 (Eq. 2) was then routed over the entire catchment. Thus, separate sedigraphs for each source class were obtained
255 at the outlet of the catchment and the contribution of each source class to total sediment flux could be calculated
256 for every time step. The rain erodibility coefficient α of each geological class was estimated from the available
257 observed time series of suspended sediment concentrations (SSC), discharge and rainfall. Using the discharge and
258 SSC, the suspended sediment flux was calculated and integrated over time for each recorded event to obtain event
259 suspended sediment yield SSY_{ev} [g]. The value of α [$g\ mm^{-1}\ m^2$] was estimated separately for every event and
260 every source as:

$$261 \quad \alpha_{s,ev} = \frac{SSY_{s,ev}}{R_{ev} A_s} \quad (3)$$

262 where A_s is the erodible surface of the respective source and R_{ev} [mm] is the amount of effective rainfall during
263 the respective event. $SSY_{s,ev}$ is the contribution of source s to SSY_{ev} and was calculated based on the mean source
264 contributions. They were estimated with sediment fingerprinting in the Claduègne catchment by Uber et al. (2019)
265 and in the Galabre catchment by Legout et al. (2013). An average value of α_s was calculated by averaging over all
266 the available observed events (Table 1). As the focus of this study is on choices made during model set-up and
267 how structural connectivity is represented, a synthetic triangular hyetograph (duration of 12 h, maximum intensity
268 of 5 mm h⁻¹) representing effective precipitation (i.e. R-I) is applied spatially homogeneous over the entire
269 catchment. The simulated time is 24 h, including 12 h of rain and 12 h for the fluxes to reach the outlet.

270

271 3.4. Study design and modeling scenarios

272 To achieve the first objective dealing with the impact of modeling choices on the temporal dynamics of modeled
273 hydro-sedimentary fluxes, a one-factor-at-a-time sensitivity analysis (Pianosi et al., 2016) was conducted. The
274 model was set-up and parameterized in a basic scenario (Table 2, Sc.1) and then subsequently two different input

275 factors were varied: the CDA threshold to define the river network (Sc. 2) and Manning's roughness parameter n
276 (Sc. 3). Based on preliminary studies that are not reported here, these two factors were found to be the most
277 important ones in determining sediment flux dynamics. While other factors (erodibility, rainfall intensity) crucially
278 influence absolute values of erosion and suspended sediment concentration, their values are less important to
279 determine arrival times and temporal dynamics of source contributions. For the second objective dealing with the
280 impact of the location of erosion zones, indicators of structural connectivity of the two catchments are used to
281 describe the configuration of each sediment sources in the catchments. They are compared to the modeled hydro-
282 sedimentary fluxes both qualitatively by visual analyses and quantitatively by means of the calculation of
283 characteristic times of the hydrographs and sedigraphs (e.g. time of concentration, lag time). To this end, another
284 set of scenarios was generated where the sediment sources were subdivided into more or less connected zones
285 (Table 2, Sc. 4).

286 The underlying hypothesis is that both modeling choices (notably CDA threshold and Manning's n) and catchment
287 characteristics (structural connectivity of the sources) determine travel times from the sources to the outlet. With
288 the presented study design, it could be assessed whether modeling choices or actual catchment configurations were
289 more important in generating temporal variability in sediment outputs.

290

291 ***Sc.1: Basic scenario***

292 In the basic scenario the threshold to define the river network was set to 15 ha and the sources were classified
293 according to their geology as in the sediment fingerprinting studies. In the "river network" modeling units,
294 Manning's n was set to 0.05 and in the "hillslopes" and "badlands" modeling units it was set to 0.8. The value in
295 the river network corresponds to what can be expected from values reported in the literature for streams comparable
296 to the Claduègne and the Galabre (Te Chow, 1959; Barnes, 1967; Limerinos, 1970). For the values on the hillslopes
297 there are fewer recommendations from the literature as the use of the St. Venant equations for the calculation of
298 fluxes on hillslopes is much less common. Existing studies indicate that the values have to be considerably higher
299 than those used commonly in river flow models (Engman et al., 1986; Hessel et al., 2003; Fraga et al., 2013;
300 Hallema et al., 2013). As these values are uncertain, the impact of this parameterization was assessed in further
301 scenarios. The basic scenario was used as the main reference to compare the other scenarios to and for the
302 comparison between the two catchments.

303 ***Sc. 2: Impact of the CDA threshold***

304 We tested the impact of varying the CDA threshold on the modeled hydro-sedimentary response while keeping all
305 other parameters unchanged compared to the basic scenario (one-factor-at-a-time sensitivity analysis). As different
306 values for Manning's n were applied in the "river network" modeling unit on one hand and in the "hillslopes" and
307 "badlands" modeling units on the other hand, the travel times of the sediments from source to sink vary depending
308 on the length of the river network in the model. Thus, it can be assumed that modeled sediment dynamics are
309 sensitive to this parameter. Five values of the CDA threshold were used: 15, 35, 50, 150 and 500 ha.

310 ***Sc. 3: Impact of the parameterization of Manning's n***

311 As the first objective of this study is to assess the impact of choices made during model set-up on the simulated
312 sediment flux dynamics, the model was run with different values of Manning's n in the "river network" modeling
313 unit on one hand and in the "hillslopes" and "badlands" modeling units on the other hand. In the river network

314 units, values were varied spanning a range from 0.025 to 0.100. This corresponds to the full range of plausible
315 values (Te Chow, 1959; Barnes, 1969; Limerinos, 1970). In the “hillslopes” and “badlands” modeling units, the
316 value of 0.8 used in the basic scenario is already at the upper end of values reported in the literature (e.g. Te Chow,
317 1959; Engman, 1986; Hessel et al., 2003; Hallema et al., 2013). Thus, values in the range of 0.2 to 0.8 were tested.

318 **Sc. 4: Source classification based on connectivity**

319 In order to test how the spatial distribution of the sources in the two distinct catchments contribute to the modeled
320 sedigraph at the outlet, the geological sources were classified into subclasses based on their distance to the outlet
321 (Sc 4a,c) and distance to the stream (Sc 4b,d). These two measures serve as a proxy for the structural connectivity
322 of the sources. The underlying hypothesis is that depending on their connectivity, several patches of the same
323 source have different travel times to the outlet and can therefore lead to several peaks in the sedigraph of the
324 source. In Sc 4b and 4d, the geological sources were classified in two groups based on their distance to the stream.
325 The badland sources in both catchments were classified as being directly adjacent to the stream network or not.
326 The diffuse sources in the Claduègne catchment, i.e. cultivated soils on basaltic and sedimentary geology, were
327 classified using a threshold of distance to the stream of 150 m. In Sc 4a and 4c, the geological sources were
328 classified in one to four groups depending on their distribution to the outlet (Figures 2a and 2c). Besides the values
329 for Manning's n used in the basic scenario, in Sc. 4c and 4d we used values for Manning's n that were less contrasted
330 between the hillslopes and the river network. This was done to assess whether the interpretation of Sc.4a and 4b
331 depended on the values of n. It should be stressed that this source classification does not influence model physics,
332 i.e. total sediment yield from a source (close + distant sources) remains the same as in the basic scenario where
333 they are not differentiated.

334 **3.5.Comparison of scenarios**

335 Modeled outputs for each scenario can be accessed and visualized through Uber et al. (2020). To assess the impact
336 of the changes done in each scenario with respect to the basic scenario, several characteristics of the modeled
337 hydrograph and sedigraphs of all sources were calculated. The lag time of liquid discharge $T_{lag,Ql}$ is calculated as
338 the time between the barycenter of the hietograph and the barycenter of the hydrograph. The time of concentration
339 of liquid discharge $T_{c,Ql}$ is defined as the time between the end of effective precipitation and the end of the outlet
340 hydrograph. A third characteristic time, $T_{spr,Ql}$, was defined to assess the spread of the hydrograph and thus, a
341 characteristic duration of the flood event (Figure 3). All of these measures were also calculated for solid discharge
342 ($T_{lag,Qs}$, $T_{c,Qs}$, $T_{spr,Qs}$) and for each source separately. Further, maximum liquid discharge $Q_{l,max}$ and solid discharge
343 $Q_{s,max}$ were determined for each scenario. Our simulations were truncated 12 h after the end of precipitation and in
344 some cases fluxes did not recede to zero, so a threshold of 0.1 Q_{max} was used to calculate T_{lag} , T_c and T_{spr} for solid
345 and liquid discharges. We use these metrics to quantitatively assess differences in model output between the
346 scenarios described above.

347

348 **4.Results and discussion**

349 **4.1.Impact of modeling choices on modeled sediment dynamics**

350 ***Varying the contributing drainage area threshold***

351 Results show that modeled hydrographs and sedigraphs were sensitive to the choice of the CDA threshold used to
352 define the river network. Figure 4 shows the modeled hydrographs that were obtained when the CDA threshold
353 was varied from 15 to 500 ha. For both catchments, higher values led to a less steep rising limb of the hydrograph,

354 lower and later peak flow, slower recession and a flatter hydrograph (Figure 4a,c). Thus, the lag time T_{Lag} , time of
355 concentration T_c and time of spread T_{spr} of liquid discharge increased with increasing CDA threshold (Figure
356 5a,b,c; Table 3). In both catchments, the hydrographs obtained with thresholds of 15, 35 and 50 ha were relatively
357 similar, but the results obtained with 150 and 500 ha differed considerably. In the Claduègne catchment peak flow
358 was reduced by approximately a factor 2 when the threshold was increased from 15 to 500 ha, while in the Galabre
359 catchment it decreased by about 20% (Table 3). In the Claduègne catchment the hydrograph obtained with the
360 threshold of 500 ha was much flatter than the one in the Galabre catchment and the recession was very slow, so
361 that even 12 h after the end of precipitation, discharge at the outlet persisted. This was not the case in the Galabre
362 catchment.

363 The different hydrological response could not be attributed to the difference in size of the catchments alone,
364 because a subcatchment of the Claduègne that has the same size as the Galabre catchment and a similar mean slope
365 than the entire Claduègne catchment (mean +/- sd: 25 +/- 32 %) also had a less steep rising limb of the hydrograph
366 than the Galabre (Figure 4b). The T_{Lag} of 3.2 h (basic scenario) was smaller than the one of the Claduègne
367 catchment at the outlet (4 h) but also considerably larger than the one of the Galabre catchment (2.3 h). Thus, we
368 assume that the fast rise and recession of the hydrograph in the Galabre catchment were mainly due to the steeper
369 slopes in this catchment (Table 1) given that the lengths of the river networks are similar. This is coherent with the
370 presumption that catchment response times are negatively correlated with catchment slopes (Gericke and Smithers,
371 2014). The modeled response of the sedigraphs were also very sensitive to the CDA threshold. T_{lag} , T_c and T_{spr} of
372 solid discharge increased generally with increasing CDA threshold, in particular from 150 to 500 ha (Figure 5a,b,c;
373 Table 3). Nevertheless, the changes of CDA did not affect the sedigraphs similarly for each sediment source. In
374 the Claduègne catchment, the sedigraphs obtained with CDA thresholds of 15, 35 and 50 ha were similar to each
375 other, but when larger values were used, they varied substantially for each sediment source (Figure 6a,b,c,d). In
376 particular, the sedigraphs of the basaltic and sedimentary sources were considerably delayed when the 500 ha
377 threshold was used. In the Galabre catchment the sedigraphs of all sources were highly sensitive to significant
378 changes of the CDA threshold with changes in T_{lag,Q_s} and T_{c,Q_s} of more than 100% for the CDA threshold of 500ha
379 (Table 3). When the threshold of 500 ha was used, the shape of the sedigraph of some sources differed. Indeed,
380 for the badlands in the Claduègne catchment and the black marls and the molasses in the Galabre catchment, the
381 single peak sedigraph turned into a multi peak sedigraph (Figure 6).

382 The differences in the modeled sedigraphs when different values for the CDA threshold were used were also
383 obvious when the simulated contributions of the sources to total suspended sediment load were regarded (Figure
384 7 and [interactive figures](https://shiny.osug.fr/app/EROSION_MODEL.2020) at https://shiny.osug.fr/app/EROSION_MODEL.2020). Increasing the CDA threshold
385 from 15 to 500 ha notably prolonged the first flush of black marl dominated sediment in the Galabre catchment
386 (marked as “1” in Figure 7c,d). During the rising limb of the hydrograph and peak flow (marked “2”), the source
387 contributions were variable while they remained relatively constant during the recession period (“3”) when the
388 CDA threshold of 500 ha was used. This was not the case when the threshold was set to 15 ha. In this case, the
389 contribution of molasses decreased steadily throughout the event while the one of limestone and quaternary
390 deposits increased (“2”, “3”, and “4” in Figure 7c). In the Claduègne catchment notably the arrival of the basaltic
391 sources at the outlet was much delayed when the CDA threshold of 500 ha was used compared to when the one of

392 15 ha was used. The shape of the sedigraph with multiple peaks that was modeled with a threshold of 500 ha
393 resulted in a slower and less steady recession of the badland sources (Figure 7b).

394 Overall, our results showed that the thresholds of 15, 35 and 50 ha produced very similar results. Thus, in this
395 range, the model was not very sensitive to the CDA threshold. The parameters given in Table 3 changed by a
396 maximum of 37% compared to the basic scenario. Other authors have shown that the CDA thresholds can vary
397 spatially (i.e. different values are found in different subcatchments) and temporally (CDA thresholds vary between
398 seasons or between events; Montgomery et al., 1993; Bischetti et al., 1998; Colombo et al., 2007). In the studied
399 catchments, variability in this range seemed not to be of prime importance. However, the larger thresholds of 150
400 and 500 ha changed the modeled sediment dynamics considerably (changes of up to 280% with respect to the basic
401 scenario and several parameters changed $> 150\%$, Table 3). This result showed that it is important to use a CDA
402 threshold that is in the same order of magnitude as the value that produces a realistic river network. Field
403 observations or detailed maps (i.e. topographic map at scale 1:25000) can be valuable sources of information for
404 this purpose. The sensitivity of model output to variations of the CDA threshold was also observed by other authors
405 (Pradhanang and Briggs, 2014). For our modeling set-up it is reassuring that model results converged when the
406 CDA threshold used is derived from field observations.

407 *Varying Manning's n*

408 Changing Manning's n influenced the timing, the peak and the spread of both liquid discharge and total suspended
409 sediment load (Figure 8, Table 3). In general, increasing n_{river} and n_{hillsl} led to a later time of rise of the hydrograph,
410 a later time of peak and to slower recession with longer $T_{lag,Ql}$ and $T_{c,Ql}$ (Figure 5, Table 3). Nevertheless Q_{max} ,
411 $T_{lag,Ql}$, $T_{c,Ql}$ and $T_{spr,Ql}$ were less sensitive to changes of n_{river} and n_{hillsl} in the Galabre than in the Claduègne
412 catchment (Figure 5, Table 3). While increasing n also led to less maximum liquid discharge, this was not the case
413 for solid discharge. Peak solid discharge even increased with increasing n_{river} in the Claduègne catchment and to a
414 lesser degree also in the Galabre catchment (Table 3). Interestingly, in the Claduègne catchment liquid discharge
415 was more sensitive to changes in n_{hillsl} than to n_{river} while solid discharge was more sensitive to n_{river} . This was not
416 the case in the Galabre where both liquid and solid discharges were more sensitive to n_{hillsl} .

417 Changing Manning's n also influenced the temporal dynamics of source contributions. A low n_{hillsl} of 0.2 led to a
418 multi-peaked sedigraph in the Claduègne catchment (Figure 8b). This difference in the shape of the sedigraph also
419 led to a difference in the modeled temporal dynamics of the percentage of source contributions (Figure 9a). When
420 n_{hillsl} was set to 0.2, the decrease of the contribution of the badland sources to total suspended sediment load in the
421 Claduègne catchment was slower during the main part of the event (marked "2" in Fig 9a) and the break point
422 between phase 2 and 3 in the decrease of the badland source was more pronounced than in the basic scenario where
423 n_{hillsl} was set to 0.8 (Figure 7a). In fact, for several hours during phase 2, the contributions of the three sources
424 were nearly constant. This was not the case for the scenarios 3b and 3c where n_{hillsl} was set to 0.4 and 0.6. These
425 scenarios hardly differed from the basic scenario (see [interactive figures](#)). In the Galabre catchment the scenarios
426 3b and 3c also hardly differed from the basic scenario. When n_{hillsl} was set to 0.2, the contributions during the
427 main part of the event ("2" in Figure 9b) remained more stable in time than in the basic scenario (Figure 7c).

428 Changing n_{river} hardly changes the dynamics of the modeled source contributions in both catchments (see
429 [interactive figures](#)). In the Claduègne catchment, increasing n_{river} from 0.025 to 0.1 generally increased $T_{lag,Qs}$ and
430 $T_{c,Qs}$ (Figure 5, Table 3) and led to a slight prolongation of the first flush of sediments from the sedimentary source.

431 In the Galabre this was also the case for the first flush of sediments originating from black marl, as it was the case
432 for the changes in the CDA threshold shown in figure 7d.

433 Our results showed that even though modeled liquid discharges were sensitive to n_{hillsl} (e.g. maximum liquid
434 discharge changed by 24% in the Claduègne catchment and 12% in the Galabre catchment), the sedigraphs of the
435 main sources and thus of total suspended solid discharge were much less sensitive to this parameter (maximum
436 solid discharge changed by 3% in the Claduègne catchment and by 1% in the Galabre catchment, Figure 8). This
437 was due to the fact that in both catchments the main sediment sources were located close to the river (Table 1,
438 Figure 2). Thus, only a small fraction of the trajectory of particles was located on the hillslopes. This was also
439 represented in the modeled dynamics of the source contribution which barely changed unless the most extreme
440 value of 0.2 was applied. This result suggests that it is sufficient to have a rough idea of the value of Manning's n
441 to study the dynamics of sediment fluxes. In the Claduègne catchment the modeled sedigraph was affected by
442 variations of n_{river} which was less true for the Galabre catchment. This might be related to the difference of slopes
443 of the river network in both catchments. Indeed, the mean slope in the river network is 2-3 times higher in the
444 Galabre than in the Claduègne catchment (Table 1), suggesting that the model was more sensitive to changes in
445 Manning's n when slopes were low. However, also in the Claduègne catchment, changes in n_{river} did not change
446 the modeled dynamics of the source contributions, which was again encouraging for the use of this type of model
447 to understand hydro-sedimentary dynamics.

448

449 **4.2. The role of structural connectivity on the dynamics of suspended sediment fluxes at the outlet**

450 The application of the same rainfall event with a similar spatial discretization and parameterization to the two
451 studied catchments (i.e. basic scenario) allowed to provide a more detailed analysis on how their respective
452 characteristics influenced their hydrosedimentary response. A first result was that the Galabre catchment reacted
453 faster than the Claduègne catchment. The hydrographs and the sedigraphs rose earlier than in the Claduègne
454 catchment. We assume that this was mainly due to the steeper slopes of the Galabre catchment (Table 1). From
455 Figures 7 and 9 a general pattern of the contribution of the different geological sources to total suspended sediment
456 load can be derived: In the Claduègne catchment at the onset of the event ("1"), the sediments originated from the
457 sedimentary source and the badlands. During the phases 2 and 3 of the event, the main source (i.e. the badlands,
458 Table 1) clearly dominated total suspended sediment load. The contribution of this source decreased gradually
459 while the percentage of contribution of the two others increased. In the Galabre catchment at the onset of the event
460 ("1"), suspended sediment originated almost entirely from the black marls, i.e. the source closest to the outlet. In
461 the second phase of the event, the main source (i.e. molasse) arrived and clearly dominated total suspended
462 sediment load. Thereafter, the contribution of the molasses decreased while the one of the limestones and the
463 quaternary deposits increased (phases 3 and 4). These general patterns were broadly consistent with the location
464 of the different geological sources in the two catchments. However, some discrepancies appear when comparing
465 the timings of arrivals of the various geological sources to the ranking of the various connectivity indicators (i.e.
466 distance to stream, to outlet, IC Borselli and IC Cavalli). The lag times of the sources in the Claduègne catchment
467 could generally be ranked as $T_{lag,Qs\ bad} < T_{lag,Qs\ sed} < T_{lag,Qs\ bas}$ (Table 3, Figure 5). This was also true for $T_{c,Qs}$
468 and $T_{spr,Qs}$ and consistent with the ranking of the mean distance to the stream as well as with both mean IC values
469 but not with the mean distance to the outlet, as the sedimentary sources were the closest from the outlet (Table 1).
470 In the Galabre catchment $T_{lag,Qs}$, $T_{c,Qs}$ and $T_{spr,Qs}$ of the molasses and marls were always smaller than the ones of

471 quaternary deposits and limestones (basic scenario, Table 3). This was coherent with the ranking of mean distances
472 to the stream but not with the ranking of mean distances to the outlet nor with the one of mean IC values (Table
473 1). Actually, the mean IC values in the Galabre were very similar for each of the four geological sources of
474 sediments and could not really be used to discriminate the sources in terms of the timing of arrivals of the
475 sedigraphs at the outlet.

476 To further address the respective roles of the distance to the outlet and the distance to the stream on the pattern of
477 source contributions to total suspended sediment load throughout events, the geological sources were subdivided
478 based on these measures in the scenarios 4a to 4b (Table 2). In this way, model output consisted of separate
479 sedigraphs for the close and distant subsources of a given source class. The sum of these sedigraphs is the same as
480 the sedigraph of that source class in the basic scenario. Figures 10 and 11 showed for the Galabre catchment that
481 the limestone sources that were close to the river and the ones that were close to the outlet exhibited a clockwise
482 discharge-sediment flux hysteresis pattern while the distant ones exhibited an anticlockwise pattern. These results
483 confirmed typical interpretations of hysteresis loops, i.e. the assumption that clockwise loops indicate a dominance
484 of close sources because maximum sediment flux occurs before peak discharge while anticlockwise hysteresis
485 patterns indicate a dominance of more distant sources (Bača, 2008; Misset et al., 2019). The results further
486 highlighted that the sedigraphs of the different sediment sources were strongly related to their location in the
487 catchments and their structural connectivity. The absence of coherent trends of the ranking of the $T_{lag,Qs}$ with the
488 one of the mean distances of the sources to the outlet could be related to the distribution of the distances to the
489 outlet of all sediment sources that were generally more scattered than the distribution of the distances to the stream,
490 particularly for the Galabre catchments (Figures 2c,d). Thus, the mean distance to the outlet was not sufficient to
491 determine travel times of the sources to the outlet. Additionally, the triangular rain applied to both catchments had
492 a rather long duration, much longer than the times of concentration of both catchments. Thus, the sedigraphs of all
493 subsources were stretched over a time span that was comparable to the time span of the rain event. The distant
494 sources arrived at the outlet long before the flux of the close sources ceased. Consequently, the sedigraphs of the
495 different subsources of both catchments were superposed and did not lead to separate peaks.

496 Even though different patches of closer and more distant subsources did not lead to multippeak sedigraphs and thus
497 to a very high flux variability, the classification into close and distant subsources from the outlet allowed to explain
498 the dynamics of source contributions. The first peak of black marls that arrived at the outlet of the Galabre during
499 the onset of the event, originated entirely from the subsources that were close to the outlet and adjacent to the river
500 network (marked “1” in Figures 10e and 11e). For the molasses and quaternary deposits, the distance to the river
501 or the outlet hardly impacted the variability of the predicted source contributions. The first molassic sediments that
502 arrived at the outlet during the rise of the hydrograph (“2”), originated almost entirely from the molassic patch that
503 was directly adjacent to the river network. However, the decrease of the contribution of the adjacent sources during
504 peak flow (“3”) occurred simultaneously with the arrival of the further sources.

505 A similar dynamic was observed in the Claduègne catchment. The first flush of sediments with a high contribution
506 from the sedimentary source, originated entirely from sedimentary sources that were directly adjacent to the stream
507 and from the badlands that were closest to the outlet (marked “1” in Figures 12e and 13e). When the results were
508 analyzed in terms of the distance to the outlet, it was remarkable that sediments which originated from the class
509 badland 3 (corresponding to a distance to the outlet of 7.5-10 km; $T_{lag,Ql} = 2.17$ h) arrived during the rising limb of
510 the hydrograph (“2”) before the ones that originated from badland 2 (distance to the outlet of 5-7.5 km, $T_{lag,Ql} =$

511 2.67 h) even though they were further away from the outlet. This was coherent with the distance to the stream.
512 While all patches belonging to the class badland 3 were directly adjacent to the river network, the ones belonging
513 to the class badland 2 were further away from the river. It should however be stressed that this finding was related
514 to the parameterization of the model and the choice of using contrasted roughness coefficients in hillslopes and in
515 the river. In the results of scenario 4c where n_{river} was set to 0.1 and $n_{hillsl.}$ was set to 0.2 (i.e. less difference between
516 n_{river} and $n_{hillsl.}$) this was not observed.

517 The fact that in both catchments different hysteresis loops were observed for subsources of different connectivity
518 showed that the subsources exhibited different hydrosedimentary behavior. It also showed that even a simple
519 classification based on the distributions of the geological sources of sediments according to their distance to the
520 stream or the outlet could help to understand the sediment flux dynamics at the outlet of mesoscale catchments.
521 Among the various connectivity indicators (i.e. distance to stream, to the outlet, IC Borselli, IC Cavalli) tested in
522 both studied catchments, the mean distances of the various geological sources to the stream were the most robust
523 proxies of the rankings of the three temporal characteristics of sedigraphs (i.e. T_{lag} , T_c and T_{spr}). Overall, our results
524 showed that the location of the sources in the catchment highly influenced the temporal dynamics of suspended
525 solid discharges at the outlet. While the two studied mesoscale catchments and also the subsources of sediments
526 within the same catchment exhibited different sensitivities to model discretization and parametrization, one main
527 result of this study was that the actual location of sediment sources and their structural connectivity were more
528 important than the modeling choices. Indeed, as soon as appropriate CDA thresholds (typically 15 to 30ha) and
529 Manning's n (in streams typically between 0.03 and 0.06 and on hillslopes between 0.4 and 0.8) were used, the
530 temporal dynamics of the modeled contributions of the different sources were relatively independent of the
531 modeling choices. Values could be varied in quite a high range without significantly changing these flux dynamics.
532 As this finding could be different for different types of rain events, notably shorter events, further studies should
533 focus on the influence of rainfall dynamics on modeled sediment fluxes in mesoscale catchments as was done
534 recently by Battista et al. (2020).

535 **5.Conclusion**

536 This study aimed to improve our understanding of hydrosedimentary processes leading to temporal variability in
537 the contribution of potential sources to suspended sediments at the outlet of two mesoscale catchments using a
538 distributed, physically based numerical model. As a first objective, we analyzed to which extent the choices made
539 during model discretization and parameterization impacted the modeled suspended sediment flux dynamics. The
540 shape and the magnitude of the modeled hydrographs and sedigraphs were sensitive to the contributing drainage
541 area threshold to define the river network and to Manning's roughness parameter n in the river network and on
542 hillslopes. However, the model was less sensitive to all three values once the parameters varied only in a restricted,
543 reasonable range. The pattern of modeled source contributions remained relatively similar when the CDA threshold
544 was restricted to the range of 15 to 50 ha, n on the hillslopes to the range 0.4-0.8 and to 0.025-0.075 in the river.
545 Then, the second objective was to assess how the location of geological sources in the catchment impacted the
546 modelled temporal dynamics of suspended sediments at the outlets. The classification of the geological sources
547 in subgroups showed that the hydrosedimentary responses differed in the two studied catchments due to the
548 combined effects of the distance from the sources to the point of entry of sediments in the river network, the
549 distance of the sources to the outlet as well as the slopes of hillslopes and rivers. Among the various structural

550 connectivity indicators tested to describe the geological sources, the mean distance to the stream was found to be
551 the most relevant proxy of the temporal characteristics of the modeled sedigraphs.

552

553

554

555 **6.Acknowledgements**

556 The authors would like to acknowledge the Ciment platform of the Université Grenoble Alps for access to
557 calculation clusters, the Draix Bléone and OHMCV long term observatories funded by the National Institute of
558 Science of the Universe for access to data sets and the OZCAR research infrastructure. The authors are grateful to
559 Laurent Bourgès, Rémi Cailletaud and OSUG for the publication of the DOI of dataset and the deployment of
560 shinyproxy on the OSUG servers to host the interactive application that enables to visualize the dataset.

561 **7.References**

562

563 Alpert, P., Ben-Gai, T., Baharad, A., Benjamini, Y., Yekutieli, D., Colacino, M., Diodato, L., Ramis, C., Homar,
564 V., Romero, R., et al. (2002). The paradoxical increase of Mediterranean extreme daily rainfall in spite of decrease
565 in total values. *Geophysical research letters*, 29(11):31-1.

566 Bača, P. (2008). Hysteresis effect in suspended sediment concentration in the Rybàrik basin, Slovakia.
567 *Hydrological Sciences Journal*, 53(1):224-235.

568 Baffaut, C., Nearing, M., Ascough II, J., and Liu, B. (1997). The WEPP watershed model: II. sensitivity analysis
569 and discretization on small watersheds. *Transactions of the ASAE*, 40(4):935-943.

570 Barnes, H. H. (1967). *Roughness characteristics of natural channels*. Number 1849. US Government Printing
571 O_ce.

572 Battista, G., Molnar, P., and Burlando, P. (2020). Modelling impacts of spatially variable erosion
573 drivers on suspended sediment dynamics. *Earth Surface Dynamics*, 8, 619–635.

574 Bhowmik, A. K., Metz, M., and Schäfer, R. B. (2015). An automated, objective and open source tool for stream
575 threshold selection and upstream riparian corridor delineation. *Environmental Modelling & Software*, 63:240-250.

576 Bischetti, G., Gandolfi, C., and Whelan, M. (1998). The definition of stream channel head location using digital
577 elevation data. *IAHS Publications-Series of Proceedings and Reports-Intern Assoc Hydrological Sciences*,
578 248:545-552.

579 Bladé, E., Cea, L., Corestein, G., Escolano, E., Puertas, J., Vázquez-Cendón, M.E., Dolz, J. and Coll, A. (2014).
580 Iber: herramienta de simulación numérica del flujo en ríos. *Revista Internacional de Métodos Numéricos para*
581 *Cálculo y Diseño en Ingeniería*, 30(1), 1-10.

582 Blanchet, J., Molinié, G., and Touati, J. (2018). Spatial analysis of trend in extreme daily rainfall in southern
583 France. *Climate Dynamics*, 51(3):799-812.

584 Boardman, J., Vandaele, K., Evans, R., and Foster, I. D. (2019). Off-site impacts of soil erosion and runoff: why
585 connectivity is more important than erosion rates. *Soil Use and Management*.

586 Borselli, L., Cassi, P., and Torri, D. (2008). Prolegomena to sediment and ow connectivity in the landscape: A GIS
587 and field numerical assessment. *Catena*, 75(3):268-277.

588 Boudevillain, B., Delrieu, G., Galabertier, B., Bonnifait, L., Bouilloud, L., Kirstetter, P.-E., and Mosini, M.-L.
589 (2011). The Cévennes-Vivarais Mediterranean Hydrometeorological Observatory database. *Water Resources*
590 *Research*, 47(7): W07701.

591 Braud, I., Ayrat, P.-A., Bouvier, C., Branger, F., Delrieu, G., Le Coz, J., Nord, G., Vandervaere, J.-P., Anquetin,
592 S., Adamovic, M., Andrieu, J., Batiot, C., Boudevillain, B., Brunet, P., Carreau, J., Confoland, A., Didon-Lescot,
593 J.-F., Domergue, J.-M., Douvinet, J., Dramais, G., Freydier, R., Gérard, S., Huza, J., Leblois, E., Le Bourgeois,
594 O., Le Boursicaud, R., Marchand, P., Martin, P., Nottale, L., Patris, N., Renard, B., Seidel, J.-L., Taupin, J.-D.,
595 Vannier, O., Vincendon, B., and Wijbrans, A. (2014). Multi-scale hydrometeorological observation and modelling
596 for flash flood understanding. *Hydrology and Earth System Sciences*, 18(9):3733-3761.

597 Brils, J. (2008). Sediment monitoring and the European Water Framework Directive. *Annali dell'Istituto Superiore*
598 *di Sanita*, 44(3):218.

599 Brosinsky, A., Foerster, S., Segl, K., López-Tarazón, J. A., Piqué, G., and Bronstert, A. (2014). Spectral
600 fingerprinting: characterizing suspended sediment sources by the use of VNIR-SWIR spectral information. *Journal*
601 *of Soils and Sediments*, 14(12):1965 - 1981.

602 Cavalli, M., Trevisani, S., Comiti, F., and Marchi, L. (2013). Geomorphometric assessment of spatial sediment
603 connectivity in small alpine catchments. *Geomorphology*, 188:31-41.

604 Cea, L. and Bladé, E. (2015). A simple and efficient unstructured finite volume scheme for solving the shallow
605 water equations in overland flow applications. *Water Resources Research*, 51(7):5464-5486.

606 Cea, L., Legout, C., Grangeon, T., and Nord, G. (2016). Impact of model simplifications on soil erosion
607 predictions: application of the GLUE methodology to a distributed event-based model at the hillslope scale.
608 *Hydrological Processes*, 30(7):1096-1113.

609 Cea, L. and Vázquez-Cendon, M. E. (2012). Unstructured finite volume discretization of bed friction and
610 convective flux in solute transport models linked to the shallow water equations. *Journal of Computational Physics*,
611 231(8):3317-3339.

612 Colombo, R., Vogt, J. V., Soille, P., Paracchini, M. L., and de Jager, A. (2007). Deriving river networks and
613 catchments at the European scale from medium resolution digital elevation data. *Catena*, 70(3):296-305.

614 Cooper, R. J., Krueger, T., Hiscock, K. M., and Rawlins, B. G. (2015). High-temporal resolution fluvial sediment
615 source fingerprinting with uncertainty: a Bayesian approach. *Earth Surface Processes and Landforms*, 40(1):78-
616 92.

617 Cossart, E., Viel, V., Lissak, C., Reulier, R., Fressard, M., and Delahaye, D. (2018). How might sediment
618 connectivity change in space and time? *Land Degradation & Development*, 29(8):2595-2613.

619 Crema, S. and Cavalli, M. (2017). SedInConnect: A stand-alone, free and open source tool for the assessment of
620 sediment connectivity. *Computers & Geosciences*.

621 Courant R, Friedrichs K and Lewy H. (1967). On the partial difference equations of mathematical physics. *IBM*
622 *journal of Research and Development*. 11(2):215-234

623 Engman, E. T. (1986). Roughness coefficients for routing surface runoff. *Journal of Irrigation and Drainage*
624 *Engineering*, 112(1):39-53.

625 Esteves, M., Legout, C., Navratil, O., and Evrard, O. (2019). Medium term high frequency observation of
626 discharges and suspended sediment in a Mediterranean mountainous catchment. *Journal of Hydrology*, 568:562-
627 574.

628 Evrard, O., Navratil, O., Ayrault, S., Ahmadi, M., Némery, J., Legout, C., Lefèvre, I., Poirel, A., Bonté, P., and
629 Esteves, M. (2011). Combining suspended sediment monitoring and fingerprinting to determine the spatial origin
630 of fine sediment in a mountainous river catchment. *Earth Surface Processes and Landforms*, 36(8):1072-1089.

631 Fraga, I., Cea, L., and Puertas, J. (2013). Experimental study of the water depth and rainfall intensity effects on
632 the bed roughness coefficient used in distributed urban drainage models. *Journal of Hydrology*, 505:266-275.

633 Fryirs, K. (2013). (dis)connectivity in catchment sediment cascades: a fresh look at the sediment delivery problem.
634 *Earth Surface Processes and Landforms*, 38(1):30-46.

635 Gaillardet, J., Braud, I., Hankard, F., Anquetin, S., Bour, O., Doriger, N., De Dreuzy, J.-R., Galle, S., Galy, C.,
636 Gogo, S., Gourcy, L., Habets, F., Laggoun, F., Longuevergne, L., Le Borgne, T., Naaim-Bouvet, F., Nord, G.,
637 Simonneaux, V., Six, D., Tallec, T., Valentin, C., et al. (2018). OZCAR: the French network of critical zone
638 observatories. *Vadose Zone Journal*, 17(1).

639 Gellis, A. and Gorman Sanisaca, L. (2018). Sediment fingerprinting to delineate sources of sediment in the
640 agricultural and forested Smith Creek watershed, Virginia, USA. *JAWRA Journal of the American Water*
641 *Resources Association*.

642 Gericke, O. and Smithers, J. (2014). Review of methods used to estimate catchment response time for the purpose
643 of peak discharge estimation. *Hydrological Sciences Journal*, 58(11):1935-1971.

644 Gourdin, E., Evrard, O., Huon, S., Lefèvre, I., Ribolzi, O., Reyss, J.-L., Sengtaheuanghoung, O., and Ayrault, S.
645 (2014). Suspended sediment dynamics in a Southeast Asian mountainous catchment: Combining river monitoring
646 and fallout radionuclide tracers. *Journal of Hydrology*, 519:1811-1823.

647 Hallema, D. W., Moussa, R., Andrieux, P., and Voltz, M. (2013). Parameterization and multi-criteria calibration
648 of a distributed storm flow model applied to a Mediterranean agricultural catchment. *Hydrological Processes*,
649 27(10):1379-1398.

650 Hancock, G., Lowry, J., Coulthard, T., Evans, K., and Moliere, D. (2010). A catchment scale evaluation of the
651 SIBERIA and CAESAR landscape evolution models. *Earth Surface Processes and Landforms*, 35:863-875.

652 Hanley, N., Faichney, R., Munro, A. and Shortle, J.S. (1998). Economic and environmental modelling for pollution
653 control in an estuary. *Journal of Environmental Management*, 52(3):211-225.

654 Heckmann, T., Cavalli, M., Cerdan, O., Foerster, S., Javaux, M., Lode, E., Smetanova, A., Vericat, D., and
655 Brardinoni, F. (2018). Indices of sediment connectivity: opportunities, challenges and limitations. *Earth-Science*
656 *Reviews*.

657 Hessel, R., Jetten, V., and Guanghui, Z. (2003). Estimating manning's n for steep slopes. *Catena*, 54(1-2):77-91.

658 Huza, J., Teuling, A. J., Braud, I., Grazioli, J., Melsen, L. a., Nord, G., Raupach, T. H., and Uijlenhoet, R. (2014).
659 Precipitation, soil moisture and runoff variability in a small river catchment (Ardèche, France) during HyMeX
660 Special Observation Period 1. *Journal of Hydrology*, 516:330-342.

661 Inglada, J., Vincent, A., and Thierion, V. (2017). Theia OSO land cover map 2106. [https://www.theia-](https://www.theia-land.fr/en/product/land-cover-map/)
662 [land.fr/en/product/land-cover-map/](https://www.theia-land.fr/en/product/land-cover-map/) [access: 26-03-2020].

663 Laflen, J. M., Lane, L. J., and Foster, G. R. (1991). WEPP: a new generation of erosion
664 prediction technology. *Journal of Soil and Water Conservation*, 46(1):34-38.

665 Legout, C., Poulenard, J., Nemery, J., Navratil, O., Grangeon, T., Evrard, O., and Esteves, M. (2013). Quantifying
666 suspended sediment sources during runoff events in headwater catchments using spectrophotometry. *Journal of*
667 *Soils and Sediments*, 13(8):1478-1492.

668 Limerinos, J. T. (1970). Determination of the manning coefficient from measured bed roughness in natural
669 channels. US Geological Survey Water Supply Papers, 1898(B):47.

670 Lopez-Vicente, M. and Ben-Salem, N. (2019). Computing structural and functional flow and sediment
671 connectivity with a new aggregated index: A case study in a large Mediterranean catchment. *Science of The Total*
672 *Environment*, 651:179-191.

673 Merritt, W., Letcher, R., and Jakeman, A. (2003). A review of erosion and sediment transport models.
674 *Environmental Modelling & Software*, 18(8-9):761-799.

675 Misset, C., Recking, A., Legout, C., Poirel, A., Cazihlac, M., Esteves, M., and Bertrand, M. (2019). An attempt to
676 link suspended load hysteresis patterns and sediment sources configuration in alpine catchments. *Journal of*
677 *Hydrology*.

678 Montgomery, D. R. and Foufoula-Georgiou, E. (1993). Channel network source representation using digital
679 elevation models. *Water Resources Research*, 29(12):3925-3934.

680 Mukundan, R., Radclie, D., and Risse, L. (2010a). Spatial resolution of soil data and channel erosion effects on
681 swat model predictions of ow and sediment. *Journal of Soil and Water Conservation*, 65(2):92-104.

682 Mukundan, R., Radclie, D. E., Ritchie, J. C., Risse, L. M., and McKinley, R. A. (2010b). Sediment fingerprinting
683 to determine the source of suspended sediment in a southern piedmont stream. *Journal of Environment Quality*,
684 39(4):1328.

685 Navratil, O., Evrard, O., Esteves, M., Ayrault, S., Lefèvre, I., Legout, C., Reyss, J.-L., Gratiot, N., Nemery, J.,
686 Mathys, N., Poirel, A., and Bonté, P. (2012). Core-derived historical records of suspended sediment origin in a
687 mesoscale mountainous catchment: the River Bléone, French Alps. *Journal of Soils and Sediments*, 12(9):1463-
688 1478.

689 Nord, G., Boudevillain, B., Berne, A., Branger, F., Braud, I., Dramais, G., G_erard, S., Le Coz, J., Legout, C.,
690 Molinie, G., Van Baelen, J., Vandervaere, J.-P., Andrieu, J., Aubert, C., Calianno, M., Delrieu, G., Grazioli, J.,
691 Hachani, S., Horner, I., Huza, J., Le Boursicaud, R., Raupach, T. H., Teuling, A. J., Uber, M., Vincendon, B., and
692 Wijbrans, A. (2017). A high space-time resolution dataset linking meteorological forcing and hydro-sedimentary
693 response in a mesoscale Mediterranean catchment (Auzon) of the Ardèche region, France. *Earth System Science*
694 *Data*, 9(1):221-249.

695 Owens, P., Batalla, R., Collins, A., Gomez, B., Hicks, D., Horowitz, A., Kondolf, G., Marden, M., Page, M.,
696 Peacock, D., Petticrew, E., Salomons, W., and Trustrum, N. (2005). Fine-grained sediment in river systems:
697 environmental significance and management issues. *River research and applications*, 21(7):693-717.

698 Palazon, L., Latorre, B., Gaspar, L., Blake, W. H., Smith, H. G., and Navas, A. (2016). Combining catchment
699 modelling and sediment fingerprinting to assess sediment dynamics in a Spanish Pyrenean river system. *Science*
700 *of The Total Environment*, 569-570:1136-1148.

701 Palazon, L., Gaspar, L., Latorre, B., Blake, W., and Navas, A. (2014). Evaluating the importance of surface soil
702 contributions to reservoir sediment in alpine environments: a combined modelling and fingerprinting approach in
703 the posets-maladeta natural park. *Solid Earth*, 5(2):963-978.

704 Panagos, P., Meusburger, K., Van Liedekerke, M., Alewell, C., Hiederer, R., and Montanarella, L. (2014).
705 Assessing soil erosion in Europe based on data collected through a European network. *Soil science and plant*
706 *nutrition*, 60(1):15-29.

707 Pandey, A., Himanshu, S. K., Mishra, S., and Singh, V. P. (2016). Physically based soil erosion and sediment yield
708 models revisited. *Catena*, 147:595-620.

709 Pianosi, F., Beven, K., Freer, J., Hall, J. W., Rougier, J., Stephenson, D. B., and Wagener, T. (2016). Sensitivity
710 analysis of environmental models: A systematic review with practical workflow. *Environmental Modelling &*
711 *Software*, 79:214–232.

712 Poulénard, J., Legout, C., Némery, J., Bramorski, J., Navratil, O., Douchin, A., Fanget, B., Perrette, Y., Evrard,
713 O., and Esteves, M. (2012). Tracing sediment sources during floods using Diffuse Reflectance Infrared Fourier
714 Transform Spectrometry (DRIFTS): A case study in a highly erosive mountainous catchment (Southern French
715 Alps). *Journal of Hydrology*, 414-415:452-462.

716 Pradhanang, S. M. and Briggs, R. D. (2014). Effects of critical source area on sediment yield and streamflow.
717 *Water and environment journal*, 28(2):222-232.

718 Tarboton, D. (2010). TauDEM (Terrain Analysis Using Digital Elevation Models). <http://hydrology.usu.edu/taudem/taudem5/> [access: 26-03-2020].

720 Tarboton, D. G., Bras, R. L., and Rodriguez-Iturbe, I. (1991). On the extraction of channel networks from digital
721 elevation data. *Hydrological Processes*, 5(1):81-100.

722 Te Chow, V. (1959). *Open-channel hydraulics*, volume 1. McGraw-Hill New York.

723 Theuring, P., Rode, M., Behrens, S., Kirchner, G., and Jha, A. (2013). Identification of fluvial sediment sources in
724 the Kharaa River catchment, northern Mongolia. *Hydrological Processes*, 27(6):845-856.

725 Tiemeyer, B., Moussa, R., Lennartz, B., and Voltz, M. (2007). MHYDAS-DRAIN: A spatially distributed model
726 for small, artificially drained lowland catchments. *Ecological modelling*, 209(1):2-20.

727 Trambly, Y., Neppel, L., Carreau, J., and Sanchez-Gomez, E. (2012). Extreme value modelling of daily areal
728 rainfall over mediterranean catchments in a changing climate. *Hydrological Processes*, 26(25):3934-3944.

729 Turcotte, R., Fortin, J.-P., Rousseau, A., Massicotte, S., and Villeneuve, J.-P. (2001). Determination of the drainage
730 structure of a watershed using a digital elevation model and a digital river and lake network. *Journal of Hydrology*,
731 240(3-4):225-242.

732 Uber, M., Legout, C., Nord, G., Crouzet, C., Demory, F., and Poulénard, J. (2019). Comparing alternative tracing
733 measurements and mixing models to fingerprint suspended sediment sources in a mesoscale Mediterranean
734 catchment. *Journal of Soils and Sediments*, pages 1-19.

735 Uber, M. (2020). *Suspended sediment production and transfer in mesoscale catchments: a new approach*
736 *combining flux monitoring, fingerprinting and distributed numerical modeling*. PhD Thesis, Université Grenoble
737 Alpes, 249 p. <http://theses.fr/2020GRALU011> [access: 24-11-2020]

738 Uber, M., Nord, G., Legout, C., Cea, L., (2020). Modeled contributions of sediment sources to total suspended
739 sediment flux in two mesoscale catchments. UGA. http://dx.doi.org/10.17178/EROSION_MODEL.2020.

740 Vanmaercke, M., Poesen, J., Verstraeten, G., de Vente, J., and Ocakoglu, F. (2011). Sediment yield in Europe:
741 spatial patterns and scale dependency. *Geomorphology*, 130(3-4):142-161.

742 Vercruyssen, K. and Grabowski, R. C. (2019). Temporal variation in suspended sediment transport: linking
743 sediment sources and hydro-meteorological drivers. *Earth Surface Processes and Landforms*.

744 Vercruyssen, K., Grabowski, R. C., and Rickson, R. (2017). Suspended sediment transport dynamics in rivers:
745 Multi-scale drivers of temporal variation. *Earth-Science Reviews*, 166:38-52.

746 Vogt, J., Soille, P., Colombo, R., Paracchini, M. L., and de Jager, A. (2007). Development of a pan-European river
747 and catchment database. In *Digital terrain modelling*, pages 121-144. Springer.

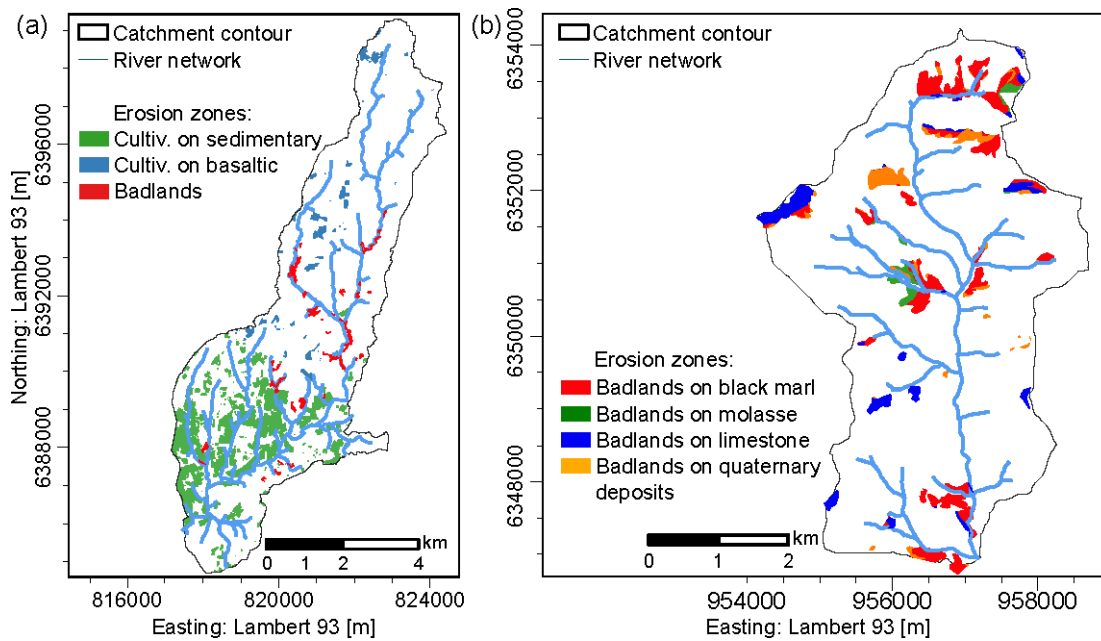
748 Wainwright, J., Parsons, A. J., Muller, E. N., Brazier, R. E., Powell, D. M., and Fenti, B. (2008). A transport-
749 distance approach to scaling erosion rates: 1. background and model development. *Earth Surface Processes and*
750 *Landforms*, 33(5):813-826.

751 Wainwright, J., Turnbull, L., Ibrahim, T. G., Lexartza-Artza, I., Thornton, S. F., and Brazier, R. E. (2011). Linking
752 environmental regimes, space and time: Interpretations of structural and functional connectivity. *Geomorphology*,
753 126(3-4):387-404.

754 Wilkinson, S. N., Hancock, G. J., Bartley, R., Hawdon, A. A., and Keen, R. J. (2013). Using sediment tracing to
755 assess processes and spatial patterns of erosion in grazed rangelands, Burdekin River basin, Australia. *Agriculture,*
756 *Ecosystems & Environment*, 180:90-102.

757 Woolhiser, D.A., Smith, R.E. and Goodrich, D.C. (1990). KINEROS—A Kinematic Runoff and Erosion Model:
758 Documentation and User Manual. Rep. No. ARS-77. USDA, Washington, D.C.

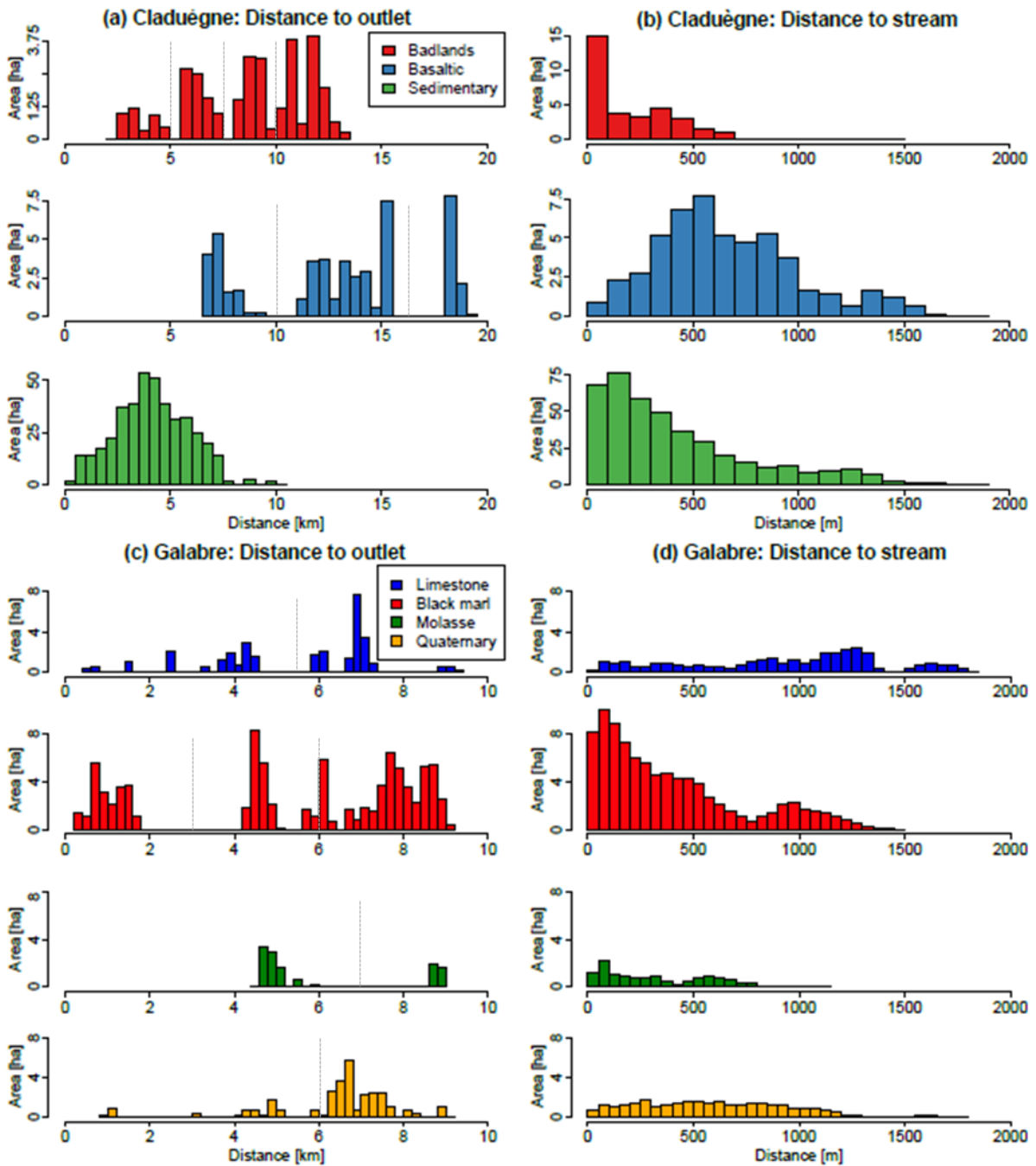
759



760

761 **Figure 1:** Maps of the (a) Claduègne and (b) Galabre catchments. Note that gypsum badlands are not considered
 762 in this study as this material is highly soluble and do not contribute to sediment fluxes. Further maps of the study
 763 sites can be found in Uber (2020).

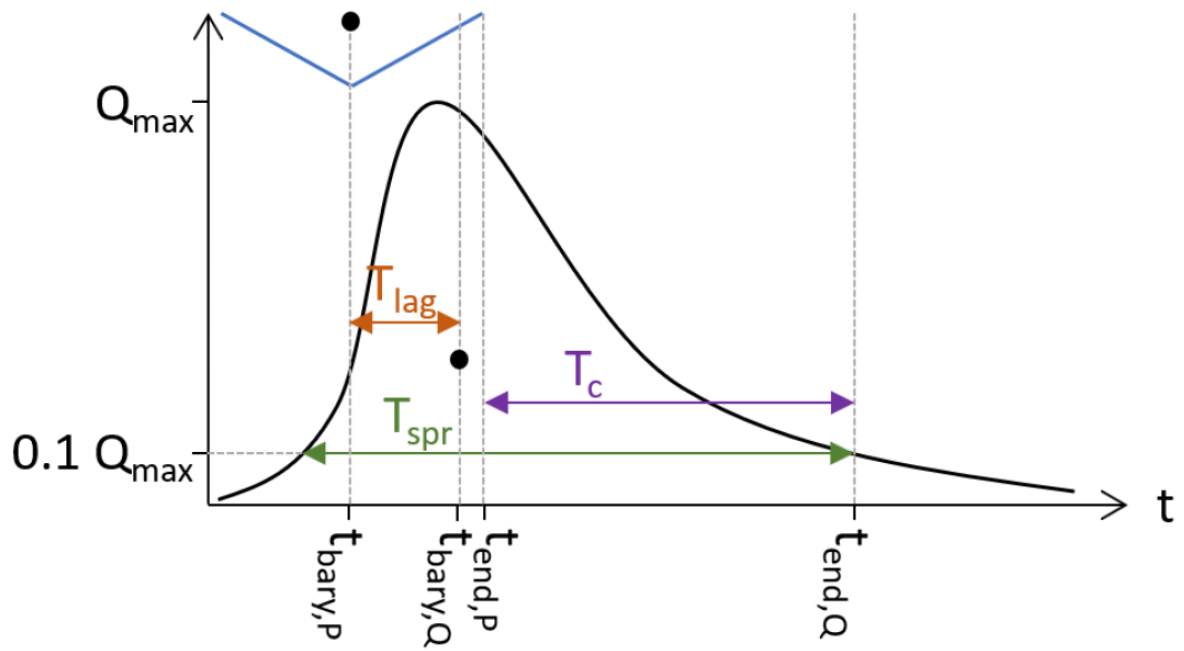
764



765

766 **Figure 2:** Distribution of the distance of the sources to the outlet (a for the Claduègne, c for the Galabre) and the
 767 stream (b for the Claduègne, d for the Galabre). The stream was defined with a threshold of contributing drainage
 768 area of 50 ha. The values represent distances along the flowlines that water and sediments travel following the
 769 gradient of the relief. Dashed grey lines correspond to the limits of subgroups of geological sources based on their
 770 distance to the outlet modeled in Sc 4b and 4d.

771

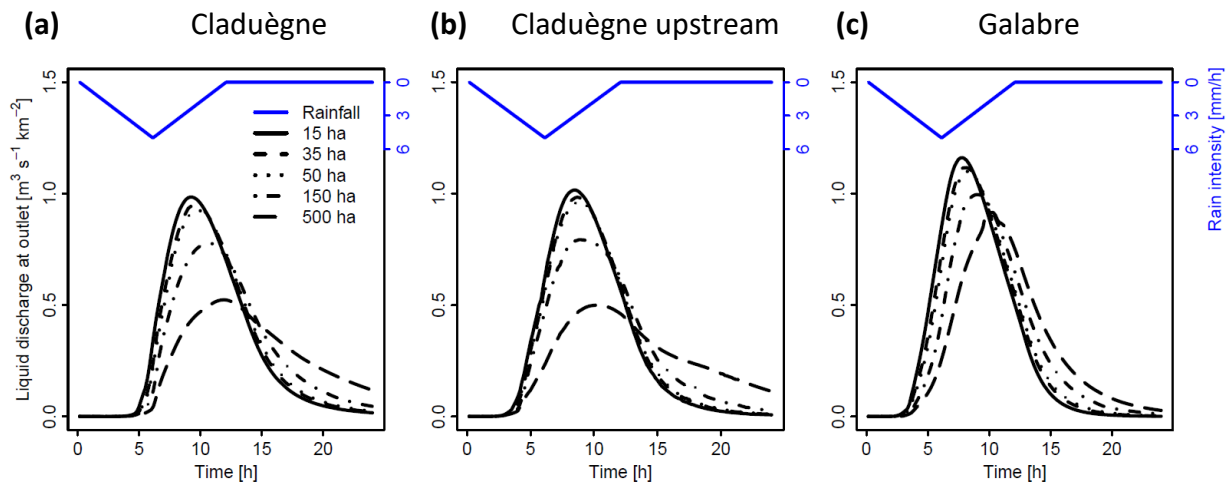


772

773

774 **Figure 3:** Scheme of the calculation of characteristic times T_{lag} , T_c and T_{spr} that were calculated using the simulated
 775 liquid and solid discharges. The points represent the barycenter of the hystograph (blue curve) and of the fraction
 776 of discharge above the threshold of $0.1 Q_{max}$ (black curve).

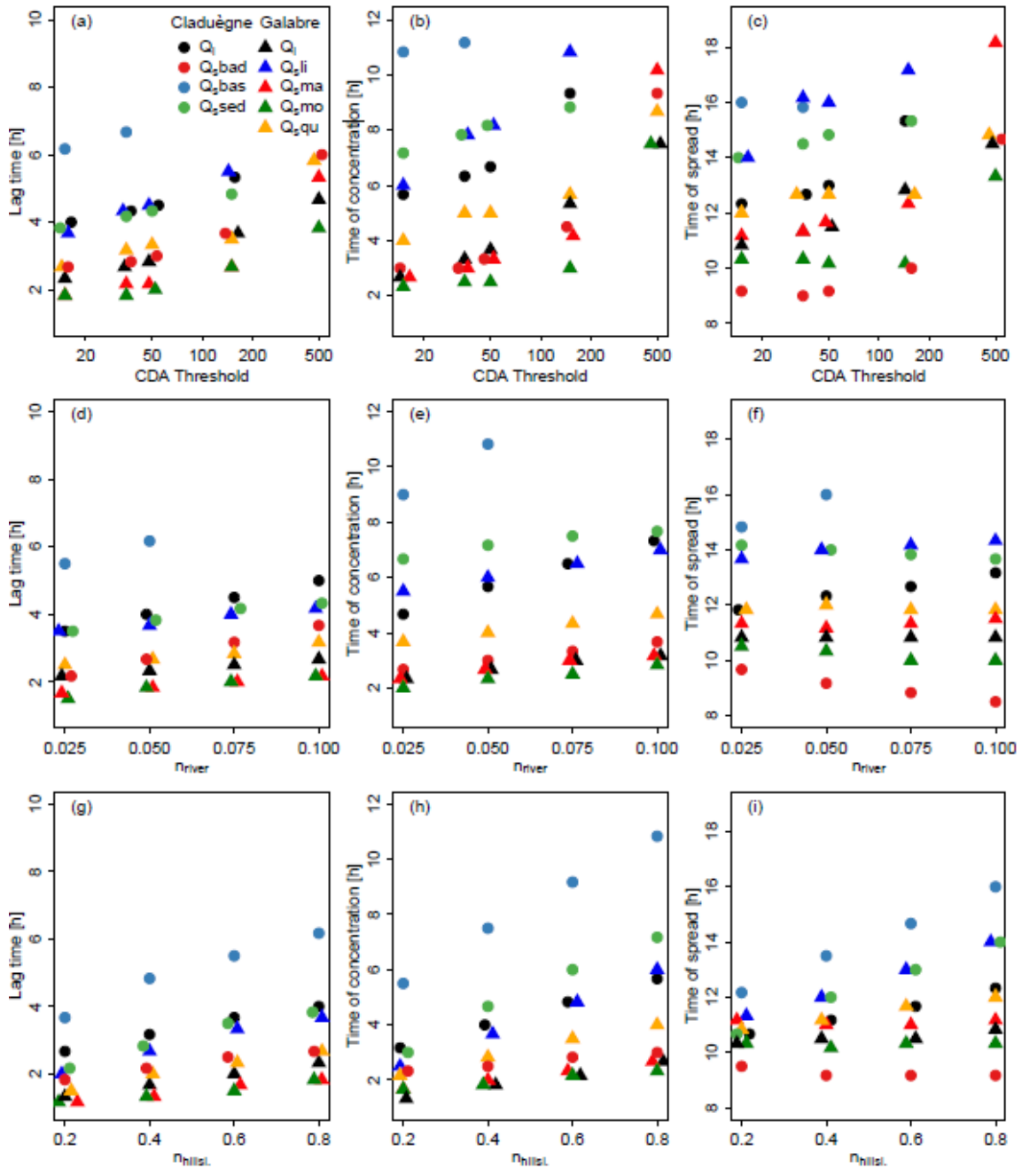
777



778

779 **Figure 4:** Simulated specific discharge obtained with different scenarios of model discretization at the outlet of
 780 (a) the 42km² Claduègne catchment, (b) the 20km² upstream outlet of the Claduègne where the size of the
 781 subcatchment is the same as the one of (c) the Galabre catchment. The threshold for defining the river network is
 782 varied from 15 ha to 500 ha.

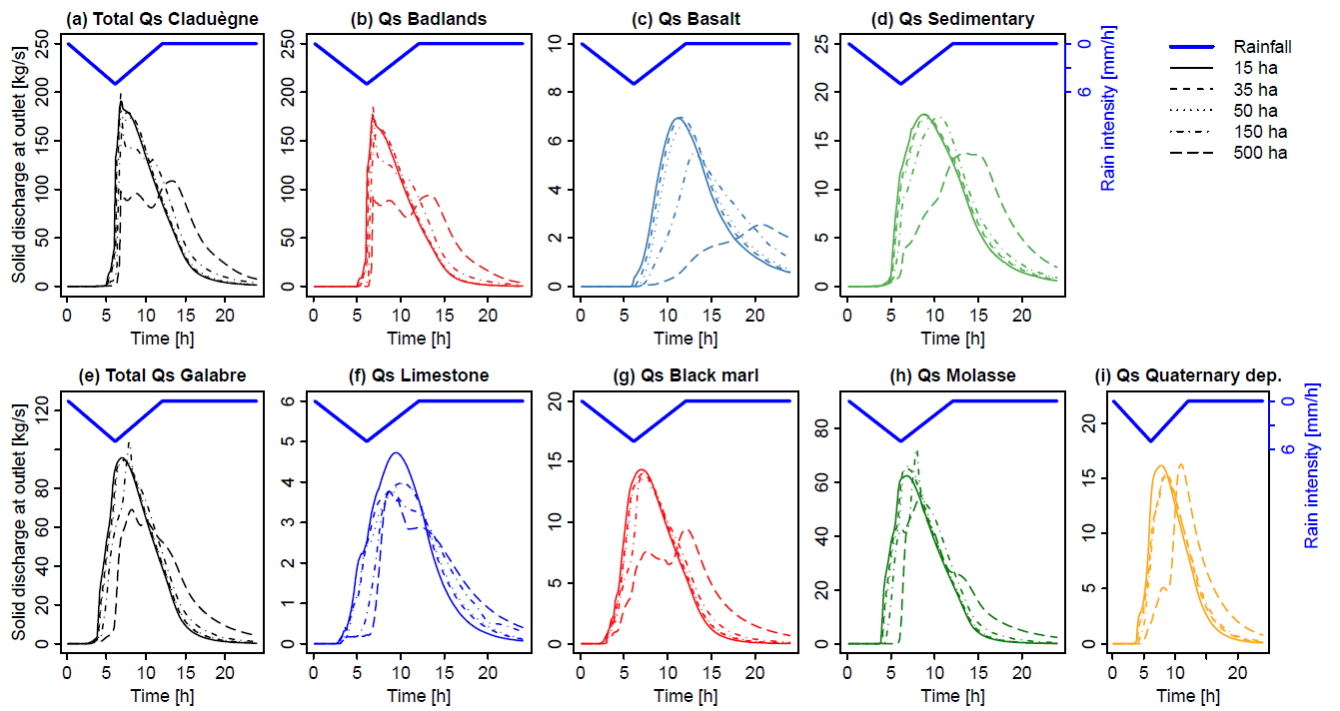
783



784

785 **Figure 5:** Sensitivity of lag times, times of concentration and time of spread to changing the CDA threshold (top
 786 row), Manning's n in the river network (middle row) and on the hillslopes (bottom row). For each catchment the
 787 characteristic times are given for liquid discharge (Q_l) and for solid discharge (Q_s) of the different source classes.
 788 Some symbols were slightly shifted on the x-axis if they were hard to see or overlapped by other symbols.

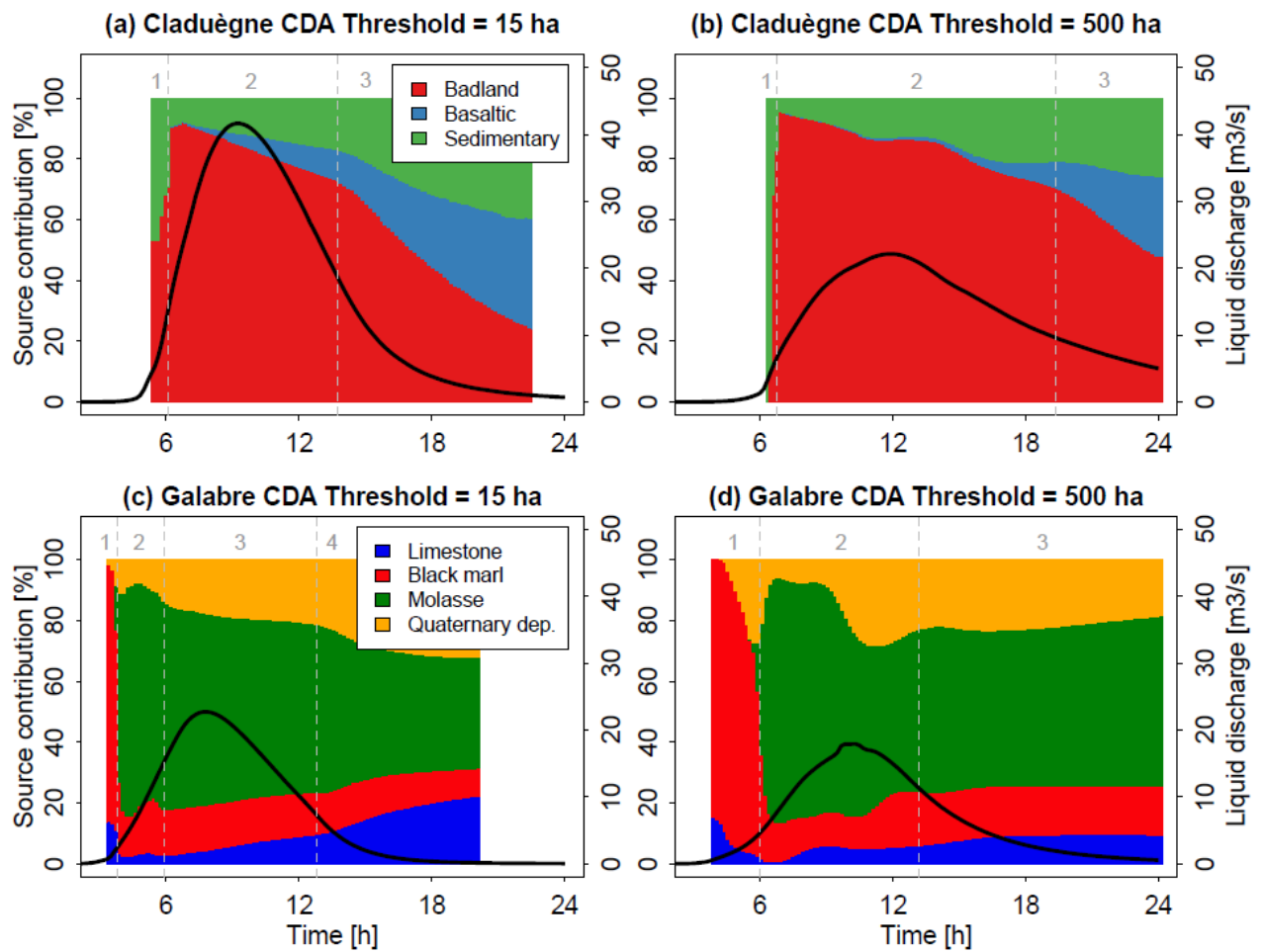
789



790

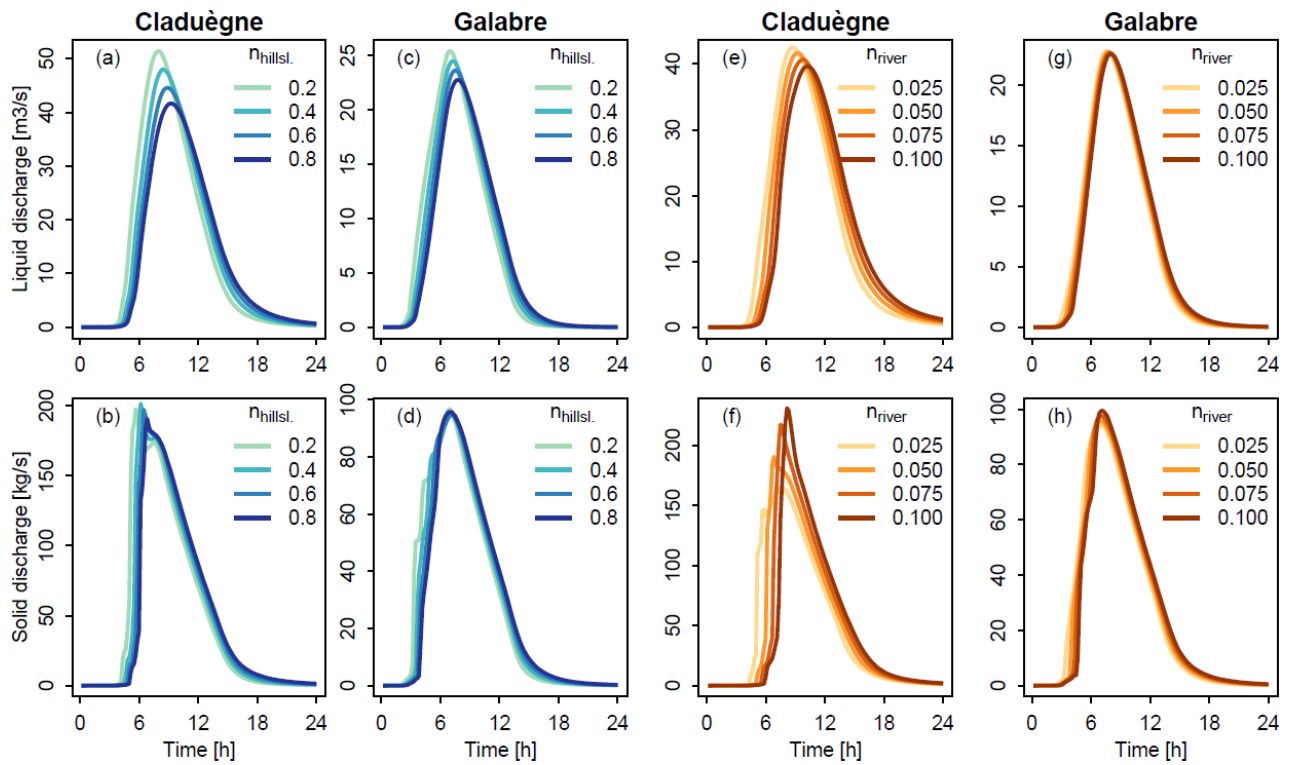
791 **Figure 6:** Simulated sedigraphs for total suspended solid discharge (Qs) and for each source in the two catchments
 792 when different values are used for the threshold of contributing drainage area (CDA) to define the river network.

793



794

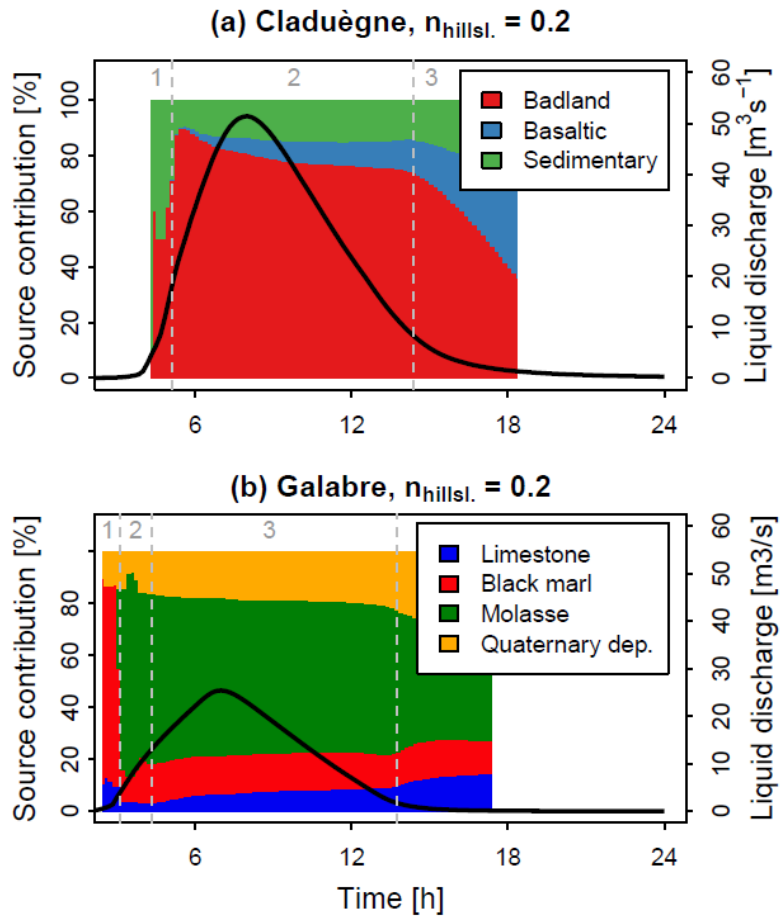
795 **Figure 7:** Modeled source contributions of the sediment sources in the Claduègne and Galabre catchments when
 796 the threshold of contributing drainage area (CDA) is set to 15 ha (left, Sc. 1) or to 500 ha (right, Sc. 2d). The color
 797 shows the contribution of the different sources to total suspended sediment load in percent. The hydrograph is
 798 additionally shown to represent the timing of the event. The results obtained with all five CDA thresholds (15, 35,
 799 50, 150 and 500 ha) for both catchments can be visualized in [interactive figures](https://shiny.osug.fr/app/EROSION_MODEL.2020) at
 800 https://shiny.osug.fr/app/EROSION_MODEL.2020



801

802 **Figure 8:** Sensitivity of modeled hydrographs (top row) and sedigraphs (bottom row) to changing Manning's
 803 roughness parameter on the hillslopes (a to d) and in the river network (e to h). For subfigures a to d n_{river} was fixed
 804 to 0.05. For subfigures e to h n_{hillsl} was fixed to 0.8.

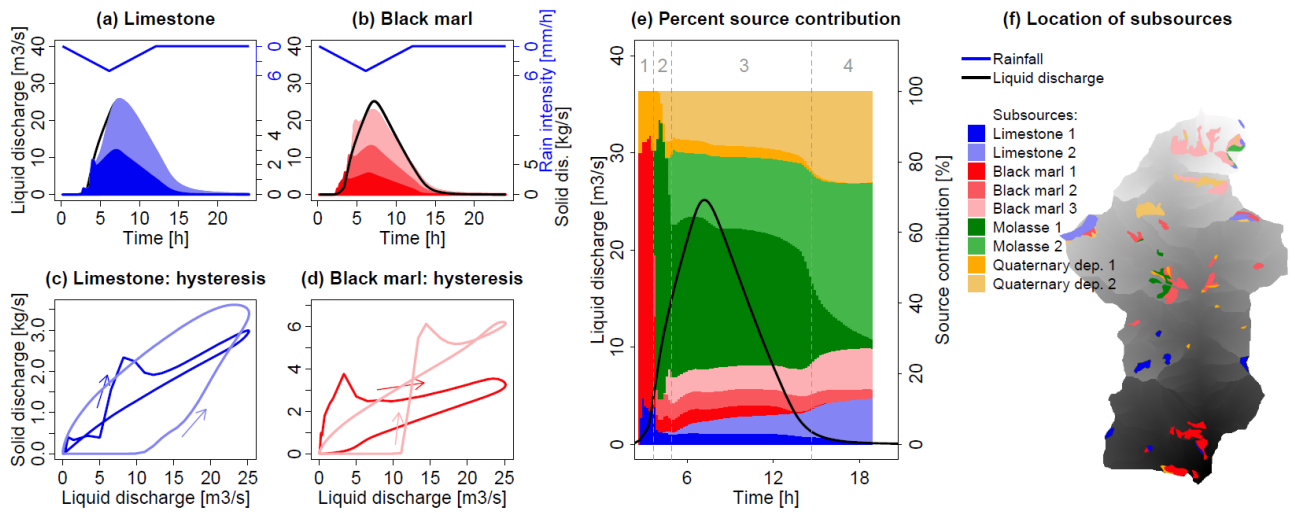
805



806

807 **Figure 9:** Modeled contributions of the sediment sources in the two catchments when Manning's n on the hillslopes
 808 was set to 0.2 (Sc. 3a). The color shows the contribution of the different sources to total suspended sediment load
 809 in percent. The hydrograph is additionally shown to represent the timing of the event. The results obtained with
 810 all roughness values for both catchments can be visualized in [interactive figures](https://shiny.osug.fr/app/EROSION_MODEL.2020) at
 811 https://shiny.osug.fr/app/EROSION_MODEL.2020

812

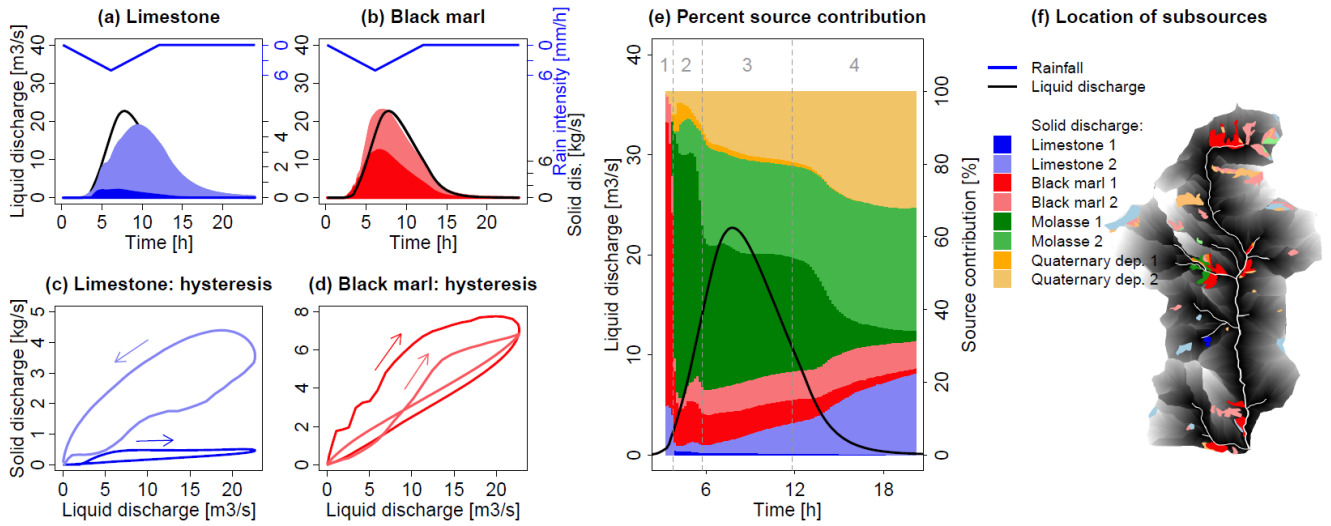


813

814

815 **Figure 10:** (a,b) Contribution of subsources of Limestone and Black marl that are classified according to their
 816 distance to the outlet (Sc. 4a). The colored areas show the contribution of sources close to the outlet (darker colors)
 817 and more distant sources (lighter colors) to the sedigraph. (c,d) shows the hysteresis loops of the subsources. (e)
 818 shows the contribution of each subsource to total suspended solid discharge in percent. The dashed lines and the
 819 grey numbers above the figure distinguish different periods of the event as referred to in the text. (f) Location of
 820 the subsources in the Galabre catchment.

821

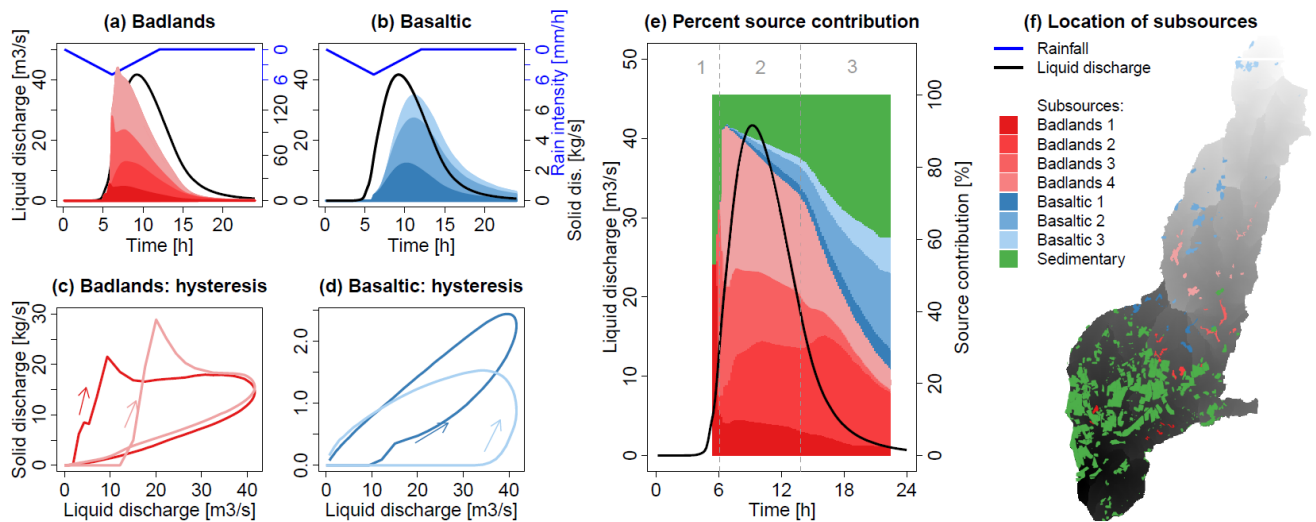


822

823

824 **Figure 11:** Contribution of subsources that are classified according to their distance to the stream in the Galabre
 825 catchment (Sc. 4b). For the description of the subfigures, see the caption of Figure 10.

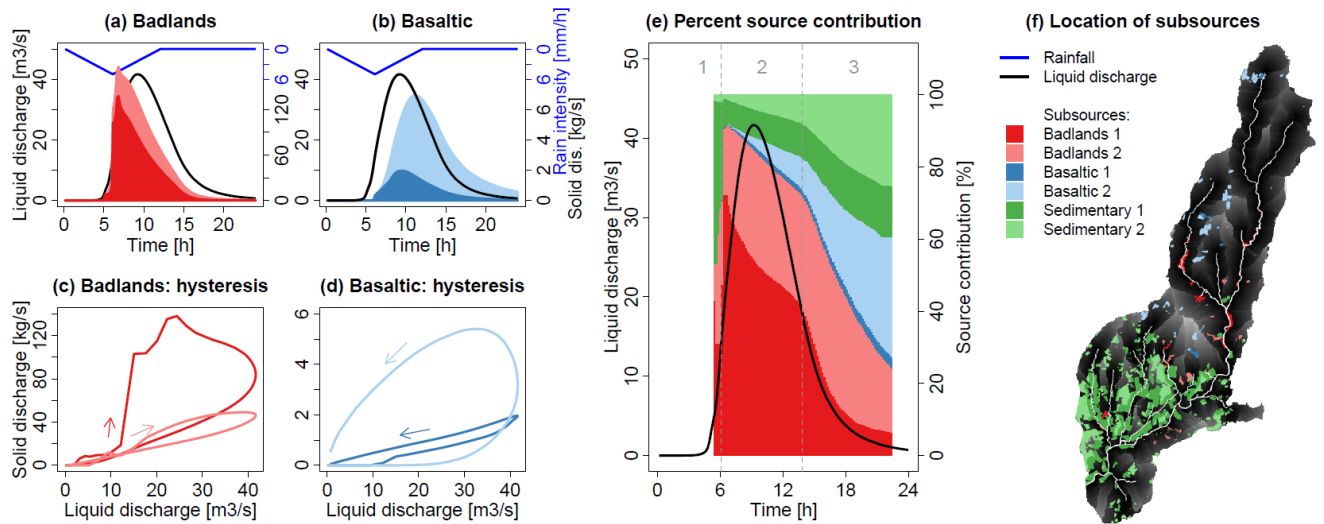
826



827

828

829 **Figure 12:** (a-b) Contribution of subsources of badlands and basaltic sources that are classified according to their
 830 distance to the outlet (Sc. 4a). The colored areas show the contribution of sources close to the outlet (darker colors)
 831 and more distant sources (lighter colors) to the sedigraph. (c-d) show the hysteresis loops of the subsources.
 832 Subfigure (e) shows the contribution of each subsource to total solid discharge in percent. The dashed lines and
 833 the grey numbers above the figure distinguish different periods of the event as referred to in the text. (f) Location
 834 of the subsources in the Claduègne catchment.



835

836

837 **Figure 13:** Contribution of subsources that are classified according to their distance to the stream in the Claduègne
 838 catchment (Sc. 4b). For the description of the subfigures see the caption of Figure 12.

839

	Cladugène				Galabre				
	Entire catchment	Badland	Basaltic	Sedimentary	Entire catchment	Limestone	Marl	Molasse	Quaternary deposits
Catchment morphology									
Area [km^2]	42.24	0.32	0.52	4.19	19.55	0.34	0.93	0.13	0.33
K_G [-]	1.87	-	-	-	1.47	-	-	-	-
Slope, hillslopes	24 ± 30	82 ± 68	11 ± 21	12 ± 13	54 ± 40	101 ± 127	67 ± 38	56 ± 30	54 ± 33
Slope, river network									
Intermittent streams	6.78	-	9.22 ^{a)}	6.06 ^{a)}	19.17	-	-	-	-
Main stream	2.72	-	4.93 ^{a)}	2.50 ^{a)}	5.71	-	-	-	-
Connectivity									
Distance to outlet [km]	9.18 ± 5.10	8.59 ± 2.82	12.91 ± 3.92	4.15 ± 1.73	4.75 ± 2.17	5.49 ± 1.99	5.28 ± 2.91	6.03 ± 1.72	6.25 ± 1.65
Distance to stream [km]	0.44 ± 0.35	0.21 ± 0.19	0.67 ± 0.34	0.42 ± 0.36	0.53 ± 0.37	0.89 ± 0.47	0.39 ± 0.35	0.34 ± 0.24	0.57 ± 0.35
IC (Borselli et al., 2008)	-9.18 ± 0.61	-8.35 ± 0.43	-9.30 ± 0.37	-8.75 ± 0.66	-8.84 ± 0.75	-7.94 ± 0.39	-7.95 ± 0.60	-8.19 ± 0.36	-8.03 ± -0.42
IC (Cavalli et al., 2013)	-5.85 ± 0.53	-5.50 ± 0.34	-6.34 ± 0.50	-5.73 ± 0.50	-4.56 ± 0.50	-4.52 ± 0.33	-4.57 ± 0.55	-4.81 ± 0.35	-4.56 ± 0.40
Erodibility									
Suspended sediment yield [$t y^{-1}$]	15947	12394	1084	2469	12856	953	1956	7474	2473
Specific yield [$t km^{-2} y^{-1}$]	380	38623	2087	589	666	2780	2113	57075	7418
Rain erodibility α^b [$g mm^{-1} m^{-2}$]	3.1	37.5	2.0	0.6	7.4	2.8	2.1	57.1	7.4

840

841

842 **Table 1:** Characteristics of the two catchments and the erosion zones. KG is Gravelius' compactness indicator
843 defined as the ratio between the catchment perimeter (P) and the one of a circle with equal surface. The values
844 given for the slopes on the hillslopes, the distance to the outlet, the distance to the streams and the two connectivity
845 indicators (IC) represent the mean +/- standard deviation. The mean slopes in the river network are given for the
846 entire network including intermittent streams (defined with a threshold of CDA of 15 ha) and for the main,
847 perennial network (CDA of 500 ha). a) The values correspond to the slope in the river network on the basaltic
848 plateau and on sedimentary geology and are not limited to the erosion zones. b) Rainfall erodibility corresponds
849 to the mass of sediment detached on 1m² by 1mm of rain (Cea et al., 2015).

850

Sc .	Th_{CDA} [ha]	Source classification	n_{river} [-]	$n_{hillsl.}$ [-]	Aim
1	15	Geology	0.050	0.8	Basic scenario
2a	35	Geology	0.050	0.8	Impact of modeling choice (spatial discretization) on the temporal dynamics of SS fluxes
2b	50	Geology	0.050	0.8	
2c	150	Geology	0.050	0.8	
2d	500	Geology	0.050	0.8	
3a	15	Geology	0.050	0.2	Impact of modeling parameterization (roughness) on the temporal dynamics of SS fluxes
3b	15	Geology	0.050	0.4	
3c	15	Geology	0.050	0.6	
3d	15	Geology	0.025	0.8	
3e	15	Geology	0.075	0.8	
3f	15	Geology	0.100	0.8	
4a	15	Geology and distance to the outlet	0.050	0.8	Impact of the location of erosion zones within the catchments on the temporal dynamics of SS fluxes
4b	15	Geology and distance to the stream	0.050	0.8	
4c	15	Geology and distance to the outlet	0.100	0.2	
4d	15	Geology and distance to the stream	0.100	0.2	

851

852 **Table 2:** Model scenarios (Sc) detailed according to the value of the contributing drainage area threshold to define
853 the river network (Th_{CDA}), the approach to classify the sources, the values for Manning's roughness parameter
854 (n) in the river network and on the hillslopes and the aim of the respective scenario.

855

	1 Basic Scenario	2a $Th_{CDA} = 35 \text{ ha}$	2b $Th_{CDA} = 50 \text{ ha}$	2c $Th_{CDA} = 150 \text{ ha}$	2d $Th_{CDA} = 500 \text{ ha}$	3a $n_{hillst.} = 0.2$	3b $n_{hillst.} = 0.4$	3c $n_{hillst.} = 0.6$	3d $n_{river} = 0.025$	3e $n_{river} = 0.075$	3f $n_{river} = 0.100$
Claduègne											
$T_{lag,Ql}$ [h]	4.00	4.33	4.50	5.33	NA	2.67	3.17	3.67	3.50	4.50	5.00
$T_{c,Ql}$ [h]	5.67	6.33	6.67	9.33	NA	3.17	4.00	4.83	4.67	6.50	7.33
$T_{spr,Ql}$ [h]	12.33	12.67	13.00	15.33	NA	10.67	11.17	11.67	11.83	12.67	13.17
$Q_{l,max}$ [$m^3 s^{-1}$]	41.65	40.16	39.14	32.91	22.14	51.44	48.00	44.57	42.51	40.67	39.64
$Q_{s,max}$ [$kg s^{-1}$]	191.04	198.67	183.24	169.41	108.65	197.45	201.52	196.98	163.88	217.06	230.97
T_{lag,Q_s} bad [h]	2.67	2.83	3.00	3.67	6.00	1.83	2.17	2.50	2.17	3.17	3.67
T_{c,Q_s} bad [h]	3.00	3.00	3.33	4.50	9.33	2.33	2.50	2.83	2.67	3.33	3.67
T_{spr,Q_s} bad [h]	9.17	9.00	9.17	10.00	14.67	9.50	9.17	9.17	9.67	8.83	8.50
T_{lag,Q_s} bas [h]	6.17	6.67	NA	NA	NA	3.67	4.83	5.50	5.50	NA	NA
T_{c,Q_s} bas [h]	10.83	11.17	NA	NA	NA	5.50	7.50	9.17	9.00	NA	NA
T_{spr,Q_s} bas [h]	16.00	15.83	NA	NA	NA	12.17	13.50	14.67	14.83	NA	NA
T_{lag,Q_s} sed [h]	3.83	4.17	4.33	4.83	NA	2.17	2.83	3.50	3.50	4.17	4.33
T_{c,Q_s} sed [h]	7.17	7.83	8.17	8.83	NA	3.00	4.67	6.00	6.67	7.50	7.67
T_{spr,Q_s} sed [h]	14.00	14.50	14.83	15.33	NA	10.67	12.00	13.00	14.17	13.83	13.67
Galabre											
$T_{lag,Ql}$ [h]	2.33	2.67	2.83	3.67	4.67	1.33	1.67	2.00	2.17	2.50	2.67
$T_{c,Ql}$ [h]	2.67	3.33	3.67	5.33	7.50	1.33	1.83	2.17	2.33	3.00	3.17
$T_{spr,Ql}$ [h]	10.83	11.33	11.50	12.83	14.50	10.33	10.50	10.50	10.83	10.83	10.83
$Q_{l,max}$ [$m^3 s^{-1}$]	22.71	21.83	21.50	19.47	17.89	25.38	24.43	23.58	22.79	22.61	22.54
$Q_{s,max}$ [$kg s^{-1}$]	95.70	94.73	94.29	103.65	69.15	96.64	95.15	94.54	94.08	97.66	99.52
T_{lag,Q_s} li [h]	3.67	4.33	4.50	5.50	NA	2.00	2.67	3.33	3.50	4.00	4.17
T_{c,Q_s} li [h]	6.00	7.83	8.17	10.83	NA	2.50	3.67	4.83	5.50	6.50	7.00
T_{spr,Q_s} li [h]	14.00	16.17	16.00	17.17	NA	11.33	12.00	13.00	13.67	14.17	14.33
T_{lag,Q_s} ma [h]	1.83	2.17	2.17	2.67	5.33	1.17	1.33	1.67	1.67	2.00	2.17
T_{c,Q_s} ma [h]	2.67	3.00	3.33	4.17	10.17	1.67	2.00	2.33	2.33	3.00	3.17
T_{spr,Q_s} ma [h]	11.17	11.33	11.67	12.33	18.17	11.17	11.00	11.00	11.33	11.33	11.50
T_{lag,Q_s} mo [h]	1.83	1.83	2.00	2.67	3.83	1.17	1.33	1.50	1.50	2.00	2.17
T_{c,Q_s} mo [h]	2.33	2.50	2.50	3.00	7.50	1.67	1.83	2.17	2.00	2.50	2.83
T_{spr,Q_s} mo [h]	10.33	10.33	10.17	10.17	13.33	10.33	10.17	10.33	10.50	10.00	10.00
T_{lag,Q_s} qu [h]	2.67	3.17	3.33	3.50	5.83	1.50	2.00	2.33	2.50	2.83	3.17
T_{c,Q_s} qu [h]	4.00	5.00	5.00	5.67	8.67	2.17	2.83	3.50	3.67	4.33	4.67
T_{spr,Q_s} qu [h]	12.00	12.67	12.67	12.67	14.83	10.83	11.17	11.67	11.83	11.83	11.83
Change [%]	0-9	10 - 19	20 - 29	30 - 49	50 - 69	70 - 89	90 - 119	120 - 149	150 - 179	≥ 180	

856

857

858 **Table 3:** Calculated characteristics of modeled hydrographs and sedigraphs for the different scenarios.
859 Abbreviations: $T_{lag,Ql}$: lag time of liquid discharge, $T_{c,Ql}$: time of concentration of liquid discharge, $T_{spr,Ql}$: spread
860 of the hydrograph, $Q_{l,max}$: peak of liquid discharge. Q_s refers to solid discharge and the characteristic times are
861 calculated for each source separately (i.e. badlands, basaltic and sedimentary in the Claduègne catchment;
862 limestone, black marl, molasses and quaternary deposits in the Galabre catchment). The background color of the
863 cells represents the percent change of each value with respect to the basic scenario. NA values indicate that the
864 hydrograph or sedigraph did not recede to 0.1 Q_{max} within the simulated time.

865

866